A cytomegalovirus immunevasin triggers integrated stress response-dependent reorganization of the endoplasmic reticulum.

Running Title: HCMV UL148 reorganizes the ER.

Hongbo Zhang[a,1], Clarissa Read[d,e,1], Christopher C. Nguyen[a,1], Mohammed N.A. Siddiquey[a], Chaowei Shang[c], Cameron M. Hall[a], Jens von Einem[d], and Jeremy P. Kamil[a,b #]

[a]Department of Microbiology and Immunology,
[b]Center for Molecular and Tumor Virology
[c]Research Core Facility
LSU Health Sciences Center, Shreveport, Louisiana, USA

[d] Institute of Virology, Ulm University Medical Center,
[e]Central Facility for Electron Microscopy, Ulm University
Ulm, Germany
[1] these authors contributed equally to the study

Running Head: HCMV UL148 Remodels the ER

#Address correspondence to Jeremy P. Kamil, jkamil@lsuhsc.edu

ABSTRACT. Human cytomegalovirus (HCMV) encodes an ER-resident glycoprotein, UL148, which activates the unfolded protein response (UPR) but is fully dispensable for viral replication in cultured cells. Hence, its previously ascribed roles in immune evasion and modulation of viral cell tropism are hypothesized to cause ER stress. Here, we show that UL148 is necessary and sufficient to drive the formation of large ER-derived structures that occupy up to 7% of the infected cell cytosol. The structures are found to be sites where UL148 coalesces with cellular proteins involved in ER quality control, such as Hrd1 and EDEM1. Transmission electron microscopy analyses reveal the structures to be comprised of tortuous, densely packed and apparently collapsed ER membranes that connect to distended cisternae. During induced ectopic expression of UL148-GFP fusion protein, punctate signals traffic to accumulate at prominent structures that exhibit poor recovery of fluorescence after photobleaching. Small molecule blockade of the integrated stress response (ISR) prevents the formation of puncta, leading to a uniform reticular fluorescent signal. Accordingly, ISR inhibition during HCMV infection abolishes the coalescence of UL148 and Hrd1 into discrete structures, which argues that UL148 requires the ISR to cause ER reorganization. Given that UL148 stabilizes immature forms of a receptor binding subunit for a viral envelope glycoprotein complex important for HCMV infectivity, our results imply that stress-dependent ER remodeling contributes to viral cell tropism.

48 **IMPORTANCE.**

49 Perturbations to ER morphology occur during infection with various intracellular
50 pathogens and in certain genetic disorders. We identify that an HCMV gene product,
51 UL148, profoundly reorganizes the ER during infection, and is sufficient to do so when
52 expressed on its own. Our results reveal that UL148-dependent reorganization of the
53 ER is a prominent feature of HCMV infected cells. Moreover, we find that this example
54 of virally induced organelle remodeling requires the integrated stress response (ISR), a
55 stress adaptation pathway that contributes to a number of disease states. Since ER
56 reorganization accompanies the roles of UL148 in HCMV cell tropism and intracellular
57 retention of the immune cell co-stimulatory ligand CD58, our results may have
58 implications for understanding the mechanisms involved. Furthermore, our findings
59 provide a basis to utilize UL148 as a tool to investigate organelle responses to stress
60 and to identify novel drugs targeting the ISR.

61 **INTRODUCTION.**

62 UL148 is a human cytomegalovirus (HCMV) ER-resident glycoprotein that plays
63 roles in evasion of cell-mediated immunity and shows intriguing effects on cell tropism.
64 During infection of epithelial cells, viruses disrupted for *UL148* replicate to produce
65 roughly 100-fold enhanced levels of infectious progeny virions compared to wildtype (1).
66 These effects correlate with reduced expression of glycoprotein O (gO), a subunit of a
67 heterotrimeric viral glycoprotein H (gH) / glycoprotein L (gL) complex (gH/gL/gO) that is
68 required for the infectivity of cell-free virions (2-4). The presence of gO in the context of
69 the heterotrimer endows the virus with the capacity to utilize the platelet derived growth
70 factor receptor α (PDGFRα) as an entry receptor (5-7). Accordingly, UL148 has been
71 found to stabilize immature forms of gO prior their assembly into gH/gL/gO
72 heterotrimers (1, 8). Despite that UL148 does not stably associate with gO, the data
73 suggest an interaction with gH (1).

74 UL148 also physically associates with CD58 (LFA-3), a co-stimulatory ligand for
75 natural killer cells and T-lymphocytes, preventing its presentation at cell surface (9).
76 Although the mechanisms by which UL148 stabilizes gO and retains CD58 within the
77 ER remain unknown, UL148 strongly contributes to activation of the unfolded protein
78 response (UPR) during infection, and is sufficient to activate the UPR when ectopically
79 expressed in non-infected cells (10). UL148 co-purifies from infected cells with SEL1L,
80 an adaptor subunit of ER-based E3 ubiquitin ligase Hrd1 that plays important roles in
81 ER-associated degradation (ERAD) of terminally misfolded glycoproteins (8). This
82 suggests a physical interaction with ERAD machinery, which may be germane to the
83 mechanism by which UL148 activates the UPR.

84 Here, we show that the expression of UL148 is necessary and sufficient to
85 induce unusual ER structures at which large quantities of ER factors involved in
86 glycoprotein quality control accumulate. In electron microscopy analyses, we find that
87 the UL148 induced ER-structures are comprised of densely packed, tortuous ER
88 membranes that form connections with tubules of highly distended cisternal space.
89 Furthermore, additional data from inhibitor studies strongly argue that ER remodeling
90 triggered by UL148 requires the integrated stress response. Overall, our results reveal
91 a striking ER perturbation induced by HCMV, and which is entirely controlled by a single
92 viral gene product. These findings may have important implications for understanding
93 how UL148 regulates viral cell tropism and/or contributes to viral evasion of cell-
94 mediated immunity.
95

96 **RESULTS.**

97

98 **UL148 causes reorganization of ER quality control proteins into unusual globular**
99 **structures.**

100 The HCMV ER-resident glycoprotein UL148 was previously observed to co-
101 localize with the ER marker calnexin during infection (1). Nonetheless, calnexin staining
102 did not show the uniform reticular pattern characteristic for the ER marker. We later
103 noticed that cells infected with a *UL148*-null virus showed uniform calnexin staining (see
104 below). To formally determine whether UL148 influences calnexin localization, we
105 compared fibroblasts at four days post-infection with either wildtype strain TB40/E virus
106 (TB_WT) or a *UL148*-null mutant (TB_148_{STOP})(8, 10), each derived from an infectious
107 bacterial artificial chromosome (BAC) clone of HCMV strain TB40/E (11) (**FIG 1**). In
108 cells infected with wildtype virus, calnexin antibodies stained unusual globular structures
109 at the cell periphery, as expected (1) (**FIG 1A, 1C, SI FIG S1A**). However, in cells
110 infected with the *UL148*-null virus, calnexin staining was uniform throughout the cytosol
111 (**FIG 1B-C**), as would be expected for an ER marker in uninfected cells. The staining
112 pattern for Hrd1, another ER marker, likewise indicated accumulation at unusual
113 globular structures during wildtype HCMV infection, but not during infection with *UL148*-
114 null mutant viruses (**FIG 1, SI FIG S1A**). Because calnexin and Hrd1 staining showed
115 uniform distribution in *UL148*-null virus infected cells, and because *UL148* is fully
116 dispensable for efficient viral replication in fibroblasts (1), these results suggest that
117 redistribution of these two ER markers depends on UL148.

118 As expected (12, 13), antibodies specific for glycoprotein H (gH), a viral envelope
119 glycoprotein, stained a juxtanuclear compartment, termed the cytoplasmic virion
120 assembly compartment (cVAC), which does not involve the ER (**FIG 1**). Similarly
121 contrasting staining patterns for Hrd1 and/or calnexin were observed in cells infected
122 with wildtype versus *UL148*-null mutants of clinical HCMV strains Merlin and TR (**FIG**
123 **S1**). Reciprocally, we restored a functional *UL148* at its native locus in the context of a
124 BAC clone of HCMV strain AD169, which spontaneously lost most of the gene in the
125 course of extensive genetic rearrangements that occurred during serial passage in
126 cultured cells. In cells infected with AD169 repaired for UL148, but not the *UL148*-null
127 parental virus, the Hrd1 staining pattern showed prominent globular structures (**FIG S1**).
128 Because similar differences in Hrd1 staining are observed between wildtype and
129 *UL148*-null infections of THP-1 macrophages, ARPE-19 epithelial cells and fibroblasts
130 (**FIG 1, FIG S1**), we concluded that UL148-dependent reorganization of ER markers
131 occurs in multiple cell types. The calnexin staining pattern seen with four different
132 primary clinical isolates from patient throat swabs likewise indicated punctate globular
133 structures. These observations, taken together with results from formal comparisons of
134 wildtype versus *UL148*-null mutants of four different BAC-cloned HCMV strains (**FIG 1,**
135 **FIG S1**), argue that UL148 profoundly affects the ER during natural infection.
136 We measured the three-dimensional volume of UL148-dependent Hrd1
137 structures from sixteen cells fixed at 96 h post infection (hpi) with strain TB40/E. On
138 average, the structures occupied 303.3 μm^3 (SEM: +/- 24.8) out of a total cell volume of
139 7657 μm^3 (SEM:+/- 651.0), which was estimated using a phalloidin-fluorophore
140 conjugate to detect the actin cytoskeleton (**FIG 1D-E**). Subtracting the volume of nuclei,

141 as indicated by 4′,6-diamidino-2-phenylindole [DAPI] (average nucleus: 1360 μm^3,
142 SEM:+/-129.4), we calculate that, on average, the structures occupy 5.2% of the
143 cytosolic volume (SEM: +/-0.61%, range: 2.0% – 7.0%). Based on these findings, taken
144 together with results comparing additional wildtype (WT) versus *UL148*-null mutant
145 HCMV strains (**FIG S1**), we conclude that the UL148-dependent ER structures are a
146 prominent feature of HCMV-infected cells.

147 UL148 substantially contributes to activation of the unfolded protein response
148 (UPR) during HCMV infection (10), and co-purifies from infected cells with SEL1L (8),
149 an adaptor subunit for the E3 ubiquitin ligase Hrd1, which plays crucial roles in ER-
150 associated degradation (ERAD) of terminally misfolded glycoprotein substrates (14).
151 Hence, the accumulation of Hrd1 and calnexin at unusual structures during wildtype but
152 not *UL148*-null infection may suggest that structures form in response to defects in ER
153 quality control (ERQC) caused by UL148. Under conditions of proteasome inhibition,
154 overexpression of certain misfolded glycoproteins causes cellular factors involved in
155 ERQC, such as calnexin, to compartmentalize from the rest of the ER, while other ER
156 markers such as BiP (Grp78) or protein disulfide isomerase (PDI) remain largely
157 unaltered (15-17).

158 To gain further insights into the nature of these peculiar ER structures, we set out
159 to develop a more comprehensive understanding of their protein composition by
160 comparing the localization of selected ER markers at 96 hpi during infection with either
161 TB_148^{HA} (1), a recombinant HCMV strain TB40/E virus that expresses UL148 fused at
162 its C-terminus to the nonapeptide epitope tag YPYDVPDYA from influenza A
163 hemagglutinin (HA), or TB_159^{HA}, a *UL148*-null comparator in which the UL148

164 homolog from rhesus cytomegalovirus, *Rh159*, likewise fused to a C-terminal HA tag, is
165 expressed in lieu of UL148.

166 We considered the TB_159^{HA} virus to be an appropriate control for the following
167 reasons. Firstly, Rh159 and UL148 exhibit ~30% identity at the amino acid level and
168 both glycoproteins localize to the ER and block cell surface presentation immune cell
169 activating ligands; UL148 retains CD58, a ligand for CD2, while Rh159 retains NKG2D
170 ligands of the MIC- and ULBP families (1, 9, 18). Secondly, Rh159 is expressed from
171 TB_159^{HA} at comparable levels and with similar kinetics observed for UL148 from
172 TB_148^{HA}, and the two viruses replicate indistinguishably in fibroblasts (**FIG 2**).
173 Moreover, as was the case in ectopic expression (10), Rh159 does not appear to
174 activate the UPR to the same extent that UL148 does, as evidenced by lower levels of
175 phospho-eIF2α and ATF4 during TB_159^{HA} infection (**FIG 2A**).

176 ERQC markers failed to coalesce into unusual structures during infection with
177 TB_159^{HA} (**FIG 3**). The structures likewise failed to occur in rhesus fibroblasts during
178 infection with a recombinant rhesus cytomegalovirus (RhCMV) that we engineered to
179 express an HA-tag fused at the C-terminus of Rh159 (**FIG S1**). The latter argues
180 against the possibility that Rh159 somehow requires the context of rhesus cells to
181 redistribute ER markers in a manner analogous to what is seen for UL148 during HCMV
182 infection. Taken together, the data suggest that UL148 and Rh159 authentically differ in
183 their effects on the secretory pathway.

184 In cells infected with TB_148^{HA}, HA antibody staining indicated localization of
185 UL148 to globular structures, as expected (1). Antibody signals from indirect confocal
186 immunofluorescence detection of cellular ER resident proteins involved in ERQC,

187 including calnexin, Hrd1, SEL1L, Herp, valosin containing protein (VCP, p97), and
188 EDEM1, strongly co-localized with signals from HA-tagged UL148 (**FIG 3-4**). These
189 results indicate that a number of ERQC factors coalesce with UL148 to form prominent
190 globular structures in infected cells. In contrast, we observed uniform ER staining
191 patterns for PDI and calreticulin (CALR), indicating that these ER markers do not
192 localize to the UL148 structures (**FIGS 3Q, 3S**). Intriguingly, antibody signals detecting
193 reticulon 3 and ribophorin 1, which are markers for smooth ER and rough ER,
194 respectively, each appreciably co-localized with UL148 (HA) signal at the induced
195 structures (**FIGS 3K, 3M)**, which indicates that the structures may involve both rough
196 and smooth ER. LC3B failed to co-localize with the structures (**FIG S2**), as might be
197 expected given that the virus inhibits macroautophagy at late times during infection (19,
198 20). Nevertheless, our results suggested that the induced structures are enriched for a
199 related mammalian ATG8 ortholog, GABARAP (**FIG 3O**).
200 In cells infected with TB_159^{HA}, all of the ER markers we examined showed
201 uniform, reticular staining, as did the anti-HA signal detecting Rh159 (**FIG 3B, D, F, H,**
202 **J, L, N, P, R, T**). EDEM1, in addition to showing reticular staining, also labeled puncta
203 associated with the nucleus (**FIG 3J, 3I**), which may represent enriched levels of the
204 protein at the rough ER membranes associated with the nuclear envelope, although we
205 cannot exclude the possibility of spurious intranuclear staining. GABARAP antibodies
206 stained the cVAC in TB_159^{HA} infected cells, but also showed a much weaker diffuse
207 signal throughout the cytosol. Even though we took steps to block viral Fc receptors,
208 which can cause rabbit antibodies to non-specifically label the cVAC (21), it is plausible
209 that GABARAP antibody signal from the cVAC reflects incomplete blocking of viral Fc

210 receptors. For both viruses, antibodies specific for the TGN marker syntaxin-6 (STX6)
211 and gH, as expected, stained the juxtanuclear cVAC structure (12, 13, 22), a post-ER
212 compartment that excludes UL148 (1) (**FIG S2**).

213 To quantify the degree of co-localization with UL148, we calculated Pearson's
214 correlation coefficients from a minimum of thirty TB_148^{HA} infected cells per staining
215 condition (fixation at 4 dpi), comparing the signal overlap for each ER marker to the HA
216 signal from UL148. The correlation coefficients (*r*) for staining patterns from antibodies
217 specific for EDEM1, Hrd1, reticulon-3 (RTN3), SEL1L, the ER retention motif KDEL, and
218 calnexin ranged from 0.8 to 0.72. These results suggest that these proteins, and
219 lumenal ER resident proteins such as BiP (GRP78) and GRP94 that contain a C-
220 terminal KDEL motif (EKDEL), extensively co-localize with UL148 at the induced
221 structures (**FIG 4**). Meanwhile, GABARAP, VCP, ribophorin-1 (RPN1), and Herp
222 showed *r* values in the range of 0.54 to 0.51, indicating a moderate degree of co-
223 localization with UL148. However, CALR and PDI, which like BiP, are lumenal ER
224 residents, and the TGN marker syntaxin-6, gave *r* values of close to zero, indicating that
225 these markers do not appreciably co-localize with UL148, as is consistent with our
226 immunofluorescence data suggesting that these markers negligibly associate with the
227 unusual structures. From these results, we conclude that the UL148-dependent ER
228 structures are enriched for cellular markers involved in glycoprotein quality control. In
229 this regard, the structures resemble the "ER quality control (ERQC) compartments"
230 described by G. Lederkremer and colleagues (15, 16, 23). We further conclude that
231 Rh159 cannot substitute for UL148 to redistribute ERQC markers.
232

233 **VCP and Hrd1 are recruited to incipient UL148 ER structures prior to calnexin.**

234 To determine whether there might be differences in the kinetics of recruitment of
235 ERQC markers during formation of the ER structures, we examined a series of time
236 points from one to four days post-infection (dpi) with wildtype HCMV strain TB40/E
237 carrying HA-tagged UL148, staining for three different ERQC markers, calnexin, Hrd1,
238 and VCP, alongside UL148 (HA). At 1 dpi the signal from UL148 was only faintly
239 detected, as expected (1), while each of the ER markers was readily detected, providing
240 a readout of their staining patterns prior to being substantially perturbed by UL148 (**FIG**
241 **S3**). At 2 dpi, we detected robust anti-HA signal, indicating the presence of UL148. At
242 this time point, UL148 exhibited intense signal at small globular puncta, which we
243 interpret to represent incipient UL148 structures, as well as more diffuse staining of a
244 reticular structure consistent with undisturbed ER. Calnexin did not appreciably co-
245 localize with the UL148 puncta until at least 3 dpi, and the structures were not readily
246 visualized by calnexin staining until 4 dpi (**FIG S3**). In contrast, signals from Hrd1 and
247 VCP staining were sufficient to mark the UL148 puncta by 2 dpi, which suggests that
248 these markers may co-localize with UL148 at earlier points during the genesis of the ER
249 structures. Notably, the appearance of Hrd1 at the structures prior to calnexin is
250 consistent with our previous results showing that UL148 co-purifies from infected cells
251 with SEL1L, an adaptor subunit for Hrd1 (8). These results imply that basal elements of
252 the ERAD machinery, exemplified by Hrd1 and VCP, might be recruited to UL148-
253 induced ER structures prior to calnexin.

254

255 **Visualization of UL148-induced ER structures by electron microscopy.**

256 To discern the ultrastructural appearance of the UL148 structures and to formally
257 ascertain their relationship to the ER, we carried out transmission electron microscopy
258 (TEM) imaging of wildtype (TB_WT) and *UL148*-null (TB_148$_{STOP}$) infected fibroblasts at
259 5 dpi. In high pressure frozen and freeze-substituted infected fibroblasts, cells with a
260 high density of viral nucleocapsids within the nucleus were selected for analysis, as this
261 feature indicates late time points during infection when UL148 is abundantly expressed.
262 The TEM results revealed prominent globular and oblong structures in the cytoplasm of
263 wildtype virus infected fibroblasts, but not *UL148*-null infected controls (**FIG 5-6**). The
264 structures stand out for their high electron-density, which may reflect the abundance of
265 ERQC proteins together with UL148 in these structures. Under higher magnification,
266 these areas are characterized by accumulations of densely packed ruffled membranes
267 and membranous material, which appear to either be collapsed ER, or ER tubules in
268 very close association with each other. The membrane accumulations were associated
269 with smooth and partially rough ER structures of seemingly enlarged cisternal space.
270 Further, tomographic reconstruction of scanning transmission electron microscopy
271 (STEM) data suggest that densely packed ER cisternae within the structures are
272 interconnected and continuous in three-dimensional space (**FIG 7B-C, SI Movie S1**).
273

274 **UL148 accumulates in a detergent-insoluble form during infection.**

275 Disease-associated variants of certain cellular proteins, such as the A103E
276 mutant of the calcium channel Orai1, and the E342K "Z" variant of alpha-1 antitrypsin (Z
277 A1AT), localize to anomalous ER structures reminiscent of those we observe to depend
278 on UL148 (17, 24-27). A103E Orai1 and Z A1AT are found to accumulate in detergent-

279 insoluble forms within the ER or within ER membranes, respectively, which indicates
280 aggregation or polymerization of these proteins, and suggests a mechanism for the
281 formation of ER structures by the proteins (17, 24, 27, 28). We therefore set out to
282 determine whether differences in solubility might correlate with the differing potentials
283 UL148 and Rh159 to cause ER reorganization and to activate the UPR (10). To
284 address this question, we infected fibroblasts with TB_148^{HA} or TB_159^{HA} at MOI 1 and
285 at various times post-infection prepared cell lysates in radioimmunoprecipitation assay
286 (RIPA) buffer. After subjecting the lysates to high-speed centrifugation, we examined
287 the relative levels of UL148 and Rh159 in the detergent-soluble supernatant and
288 detergent-insoluble pellet fractions.

289 A substantial portion of UL148 was detected from the detergent-insoluble
290 fractions at all time points tested (**FIG 8**). Furthermore, the percentage of UL148
291 detected within the insoluble fraction increased over time. In contrast, Rh159 was found
292 only in the detergent-soluble fraction. From these results, we conclude that UL148
293 accumulates in a detergent-insoluble form during infection, and that Rh159 does not do
294 so. Because the anti-HA immunoreactive band detected in both the soluble and
295 insoluble fractions from TB_148^{HA} infected cells showed a relative mobility of ~35 kD,
296 which matched that expected for the mature, endoH-sensitive glycoprotein (1), these
297 findings argue that UL148 may form aggregates or polymers within the ER.
298

299 **UL148 is sufficient to compartmentalize the ER.**

300 Our data thus far demonstrate that UL148 is necessary during infection to cause
301 redistribution of cellular ER markers for glycoprotein quality control processes, such that

302 substantial portion of the ERQC machinery appears to become sequestered away from
303 the rest of the organelle into novel membranous structures. Because a number of viral
304 proteins that remodel the ER during infection are sufficient to alter ER morphology when
305 ectopically expressed [e.g. (29),(30), reviewed in (31)], we wondered whether UL148
306 expression would be sufficient to induce ER structures akin to those seen during HCMV
307 infection. Making use of "tet-on" ARPE-19 epithelial cells that inducibly express either
308 UL148 or Rh159, each carrying a C-terminal HA-tag (32), we induced transgene
309 expression for 48 h and subsequently stained for various cellular markers for the ER, for
310 ERQC as well as for the ATG8 family proteins LC3B and GABARAP, which play roles in
311 macroautophagy and related processes.

312 In cells expressing UL148 (i148^{HA}), we observed that calnexin, Hrd1, EDEM1,
313 and VCP co-localized with UL148 at prominent globular structures reminiscent of those
314 observed during infection (**SI FIG 4**). The respective rough and smooth ER markers
315 ribophorin 1 (RPN1) and reticulon 3 (RTN3), as well as the ATG8 proteins LC3B and
316 GABARAP likewise co-localized to the UL148-induced structures. However, PDI and
317 CALR each failed to substantially co-localize with UL148 at the structures (**SI FIG 4**), or
318 at best showed only limited co-localization, consistent with our results from infected
319 cells (**FIG 3-4**). Signals from antibodies specific for the KDEL (EKDEL) motif important
320 for ER retrieval of luminal ER residents, such as BiP and GRP94, likewise showed only
321 limited co-localization with UL148. The PDI and KDEL results suggest that large
322 regions of the ER are not involved in the UL148 structures.

323 In cells expressing the UL148 homolog Rh159 (i159^{HA}), we detected uniform
324 cytoplasmic distribution of ER markers, as well as of HA-tagged Rh159, similar to what

325 we observed during infection with the recombinant HCMV TB_159^{HA} (**FIG 3**).
326 Furthermore, in this setting the staining patterns for the ATG8 family proteins LC3B and
327 GABARAP failed to indicate any notable structures. Consistent with our previous study
328 showing that UL148, but not Rh159, is sufficient to activate the UPR (10), we observed
329 accumulation of ATF4 and phosphorylated eIF2α following doxycycline (dox) induced
330 expression of UL148 but not Rh159 (**FIG 9A**). Importantly, the intensity of HA signals
331 detecting UL148 and Rh159 indicated that both ER resident immunevasins accumulate
332 at roughly comparable levels following dox induction. This argues against the possibility
333 that gross protein expression differences accounts for the differing effects of UL148 and
334 Rh159 on UPR activation and on the staining patterns for ER markers.
335 Pearson's correlation coefficient values were calculated to quantify the extent of
336 colocalization between UL148 and various cellular markers: EDEM1, Hrd1, VCP,
337 calnexin (CNX), RTN3, SEL1L, LC3B, and PDI (**FIG 9B**). The results quantitatively
338 buttress the confocal immunofluorescence results from these cells (**FIG S4**). We
339 therefore conclude that no other HCMV gene products are required for UL148 to cause
340 ERQC factors to segregate into discrete compartments. Hence, we conclude from
341 these findings that UL148 is sufficient to cause large-scale reorganization of ERQC
342 markers. Moreover, these results suggest that reorganization of ER markers into
343 discrete structures may be related to the propensity of UL148 to induce ER stress.
344 To determine whether UL148-dependent ER remodeling could be visualized in
345 real-time using live cell imaging, we constructed new "tet-on" lentiviral vectors that
346 inducibly express either UL148 or Rh159 fused at their predicted C-terminal cytoplasmic
347 tails to the enhanced green fluorescent protein (GFP) from *Aequorea victoria* (33).

348 Following lentiviral transduction, we isolated puromycin-resistant ARPE-19 and
349 subsequently subjected to fluorescence-activated cell sorting (FACS) to enrich for cells
350 that expressed GFP signal following dox treatment. The resulting cell populations,
351 which inducibly express either UL148-GFP or Rh159-GFP, were designated i148^{GFP}
352 and i159^{GFP}, respectively.

353 In live cell imaging studies, we observed that the GFP signal in dox-induced
354 i148^{GFP} cells first appeared in a reticular, largely uniform pattern, which was readily
355 visible at 5 h post-induction. However, by 9 h post-induction punctate signals began to
356 appear. These puncta were observed to traffic to sites of large-scale accumulation,
357 where large fluorescent structures progressively increased in size up until the
358 termination of the experiment at 19 h (**FIG S5, SI Movie 2**). In contrast, i159^{GFP} cells
359 exhibited a largely diffuse, reticular GFP signal at all time points monitored subsequent
360 to transgene induction (**FIG S5, SI Movie 3**). The live cell imaging results thus
361 recapitulated the differences in the HA-staining patterns observed between dox-induced
362 i148^{HA} and i159^{HA} cells following fixation, as well as those between HCMV expressing
363 HA-tagged UL148 versus *UL148*-null comparator viruses (**FIGS 1, 3, SI Fig S1**).
364

365 **UL148-GFP structures exhibit poor recovery of fluorescence after**
366 **photobleaching.**

367 To determine whether the protein contents of the UL148 induced structures
368 exhibits decreased mobility compared to non-perturbed ER regions, we carried out
369 fluorescence recovery after photobleaching (FRAP) studies. We photobleached regions
370 of GFP signal in i148^{GFP} or i159^{GFP} ARPE-19 cells that had been induced for transgene

371 expression for 24 h, and then monitored recovery of fluorescence over a 5 min time
372 period. In Rh159-GFP expressing cells (i159^{GFP}), fluorescence nearly recovered to pre-
373 bleach levels within 3 min, and by 5 min fully recovered (**SI FIG S6**). In contrast, when
374 we photobleached a prominent UL148-GFP structure, the GFP signal failed to
375 appreciably recover fluorescence during the same 5 min time period. Nonetheless,
376 regions of reticular GFP signal from an i148^{GFP} cell, which presumably represent ER
377 regions not involved in an anomalous structure, recovered fluorescent signal with
378 kinetics similar to those observed during Rh159-GFP expression. These results
379 indicate that bleached UL148-GFP within the structures cannot rapidly be exchanged
380 with UL148-GFP from other portions of the organelle, which suggests that the induced
381 UL148 structures do not exchange their contents as efficiently as unperturbed ER.
382
383 **Ectopically-expressed UL148 is degraded by proteasomes and not by autophagy.**
384 The UL148 ER structures were found to be enriched with proteins such as Hrd1,
385 SEL1L, EDEM, and VCP (**FIG 3-4**, **9B, SI FIG S4**), which are posited to play key roles
386 in ERAD, a process during which misfolded glycoproteins are recognized, processed,
387 and dislocated across the ER membrane for degradation at cytosolic proteasomes.
388 However, we also detected elements of the machinery for autophagy in close
389 association with the UL148 structures. Namely, the mammalian ATG8 ortholog
390 GABARAP co-localized with UL148 during infection (**FIG 3-4**), and both GABARAP and
391 another ATG8 ortholog, LC3B, co-localized with UL148 at the ER structures during
392 ectopic expression of UL148 (**FIG 9B, SI FIG S4**). Therefore, we wished to determine
393 whether UL148 is degraded by the proteasome, as would be consistent with

394 conventional ERAD, or by the lysosome, which would suggest a role for autophagy-
395 related processes, such as selective autophagy of the ER (34), in dispensing with
396 UL148, and presumably, in resolving the ER perturbations.

397 As a first step, we conducted a live-cell imaging "washout" experiment in which
398 i148^{GFP} cells were induced for transgene expression for 24 h, after which the growth
399 medium containing the transgene inducing agent (dox) was replaced with medium
400 lacking dox. During a 22 h imaging period following dox-washout, we observed the
401 structures to become progressively smaller as the reticular and punctate GFP signals
402 gradually abated (**SI FIG S7, SI Movie S7**). Because the results suggested that UL148-
403 GFP structures could be resolved over time, we induced UL148-GFP in tet-on ARPE-19
404 cells (i148^{gfp}) for 24 h, washed out the inducing agent (dox), and then applied either
405 epoxomicin (20 μM), an irreversible inhibitor of the proteasome (35), or folimycin (115
406 nM), a proton pump inhibitor that blocks autophagosome maturation and impedes
407 lysosome-dependent degradation (36, 37). Of the two inhibitors, only epoxomicin
408 stabilized UL148 (**SI FIG S7**). Although folimycin treatment had no obvious effect on
409 UL148-GFP levels, the drug markedly increased the levels of LC3B-II, as would be
410 expected with the lysosomal proton pump inhibitor. From these results, we conclude
411 that ectopically expressed UL148 is primarily degraded by proteasome-dependent
412 pathway.

413

414 **UL148 requires the integrated stress response to cause ER reorganization.**

415 We previously reported that UL148 triggers the UPR during ectopic expression,
416 and that UL148 contributes to activation of the PKR-like ER kinase (PERK) and inositol

417 requiring enzyme 1 (IRE1) during infection (10). The literature suggests that formation
418 of ERQC compartments requires PERK (38). PERK responds to ER stress by
419 activating the integrated stress response (ISR). In particular, PERK phosphorylates
420 eIF2α at Ser51, and the accumulation of phosphorylated eIF2α (eIF2α-P) globally
421 attenuates mRNA translation whilst stimulating the translation of a subset of mRNAs,
422 such as those encoding ATF4 and CHOP, which play roles in cellular adaptation to
423 stress (39). Stress-regulated translation of such mRNAs involves small upstream open
424 reading frames (uORFs) in their 5' untranslated regions that ordinarily suppress
425 translation under basal conditions (40, 41).

426 To examine whether ER remodeling in response to UL148 requires the ISR, we
427 turned to a well characterized small molecule inhibitor of stress-regulated translation,
428 ISRIB (42-46). ISRIB is thought to act as a "molecular staple" that holds the guanine
429 nucleotide exchange factor eIF2B in an active decameric configuration (44-47), such
430 that eIF2B will continue to generate ternary complex (eIF2•GTP•Met-tRNAi) necessary
431 for new cycles of translational initiation, despite the presence of eIF2α-P. Because
432 PERK is the kinase that phosphorylates eIF2α in response to ER stress (48, 49), we
433 also tested for effects of the PERK inhibitor GSK2606414 (50). Having confirmed that
434 ISRIB and GSK260641 do not negatively impact UL148 expression during dox-induction
435 of UL148-GFP **(FIG 10)**, we treated i148^{GFP} cells with 200 nM ISRIB, 1.1 μM
436 GSK260641, or DMSO vehicle control, and carried out live cell imaging during induction
437 of UL148-GFP expression.

438 ISRIB and GSK6060414 virtually abolished the formation of UL148 puncta
439 through 13 h post induction (dox addition), a time point at which the DMSO control

440 condition showed abundant large structures (**FIG 10C-E, SI Movies 8-10**). Based on
441 our findings (**FIG 1, 3, 5, 7, 9B, S4)**, we interpret the formation and subsequent large-
442 scale aggregation of UL148-GFP puncta to faithfully indicate ER reorganization in
443 response to UL148. Therefore, these results suggested to us that pharmacological
444 inhibition of either the ISR or PERK prevent UL148 from remodeling the ER, which
445 implies that ER remodeling in response to ER stress requires stress-regulated
446 translation.

447 Since our results with ISRIB and GSK6060414 indicated that the ISR is required
448 for ER remodeling to occur during ectopic expression of UL148, we next asked whether
449 these pharmacological agents would prevent UL148-dependent ER remodeling in the
450 physiologically authentic context of HCMV infection. Our live cell imaging studies from
451 ISRIB and GSK6060414 treatments indicated that UL148-GFP puncta could begin to
452 appear by ~19 h post treatment (**FIG 10, SI Movies 9-10**), which suggested that the
453 pharmacological activity of the drugs might diminish over time. Thus to ensure that
454 blockade of PERK and the ISR would be sustained over the 4 d period that it takes for
455 structures to fully form during HCMV infection, we replenished drug treatments every 24
456 h, replacing the spent media with media containing freshly reconstituted ISRIB,
457 GSK6060414, or DMSO vehicle control.

458 At 4 dpi, ER structures were readily visible in DMSO control treatment condition
459 but virtually abolished in the ISRIB and GSK2606414 conditions (**FIG 11A**). To quantify
460 these effects, we obtained Z-stacks from a minimum of 30 cells per treatment condition
461 and used Imaris 3D image analysis software to calculate the percentage of Hrd1 signal
462 that coalesced into discrete structures during infection. The results indicated highly

463 significant differences between the DMSO carrier alone setting compared to treatments
464 with either GSK2606414 or ISRIB (**FIG 11B**). In the DMSO control condition, on
465 average, 10% of the Hrd1 signal was found to be associated with the UL148 structures
466 (arithmetic mean; range 5.8% – 17.6%), as indicated by structures delimited by HA
467 signal detecting UL148. In the presence of ISRIB or GSK2606414, however, these
468 values were reduced to 2.8% (range: 0.69% – 7.1%) and 3.6% (range: 0.8%-6.5%),
469 respectively. Reassuringly, roughly equivalent levels of UL148 were detected in
470 Western blot analyses of protein extracts from drug treated and DMSO control
471 conditions. Therefore, differences in UL148 expression are unlikely to explain the
472 observed failure of UL148 and Hrd1 to coalesce into ER structures during inhibition of
473 either the ISR or PERK. Meanwhile, ISRIB and GSK2606414 treatments both led to
474 reduced levels of ATF4 accumulation, while the PERK inhibitor alone was able to
475 reduce the levels eIF2α-P, as indicated by a phospho-specific antibody. Therefore,
476 each of the drugs caused the expected effects on the PERK, eIF2α-P, and ATF4 axis
477 (**FIG 11C-D**).
478 A modest reduction in the levels of the viral envelope glycoprotein B (gB) was
479 observed during treatments with ISRIB or GSK2606414. This may suggest that the ISR
480 is required for optimal expression of the certain viral envelope glycoproteins. Even
481 though UL148 promotes ATF4 expression, likely via PERK activation (10), viruses that
482 lack *UL148* cause high levels of ATF4 accumulation at late times during infection, which
483 is when viral late gene products, such a gB, are expressed at their highest levels (10).
484 Hence, the activity of PERK and/or of the ISR may be required for optimal expression of
485 viral envelope glycoproteins. Regardless, the PERK inhibitor and ISRIB each prevented

486 the appearance of discrete UL148 ER structures while failing to substantially affect
487 UL148 expression. Therefore, the effects of the two inhibitors on UL148-dependent ER
488 reorganization were consistent with those seen during ectopic expression of the protein.
489 Taken together, our findings argue that the ISR is required for UL148 to cause
490 remodeling of the organelle.

491 **DISCUSSION**

492 The ER structures that we have identified are noteworthy in several regards.
493 Firstly, this example of virally-induced ER remodeling is wholly dependent on a single
494 viral gene product, UL148. Of course, there are other examples of individual viral gene
495 products that are necessary to grossly perturb ER morphology during infection which
496 are also found to be sufficient to induce such perturbations [e.g., (29, 30, 51, 52)].
497 Nonetheless, the ER structures caused by UL148 are— to the best of our knowledge, a
498 hitherto undescribed ultrastructural characteristic of the HCMV infected cell, which is
499 surprising given their size, scale, and prominence. Indeed, the average volume of the
500 structures at 96 h postinfection amounts to roughly 60% of the size of the nucleus of an
501 uninfected human fibroblast [~500 μm^3, (53)]. Although UL148 expression is
502 accompanied by UPR activation, ER reorganization occurs without killing the host cell,
503 even in the setting of ectopic expression when viral functions that inhibit programmed
504 cell death are absent. Nor does UL148 affect the yield of infectious virus during
505 replication in fibroblasts, since *UL148*-null mutant viruses replicate indistinguishably
506 from wildtype parental virus in this cell type (1, 8). As with all enveloped viruses, HCMV
507 requires the host cell secretory pathway to fold and process enormous quantities of viral
508 envelope glycoproteins that endow progeny virions with the molecular machinery for
509 infectivity. It is intriguing to consider how the infected cell tolerates spatial
510 reorganization of ER membranes and of the associated glycoprotein quality control
511 machinery without impacting the production of infectious progeny virions.

512 Furthermore, certain aspects of ER reorganization invoked by UL148 may be
513 novel to cell biology. In particular, the densely packed collapsed ER in close

514 association with varicosities that we observe to depend on UL148 during infection
515 appear to differ from the ER structures induced by other ER perturbagens. For
516 instance, a hereditary form of childhood cirrhosis caused by the *Z* allele of the alpha-1-
517 antitrypsin (Z-A1AT) gene (*SERPINA*) is characterized by polymerization of Z-A1AT
518 within the ER (26), leading to its accumulation in membrane-delimited inclusions (26,
519 27, 54). However, Z-A1AT inclusions are not observed to associate with regions of
520 collapsed ER, nor does Z-A1AT suffice to activate the UPR, even though its expression
521 sensitizes cells to other triggers of ER stress (27, 55).
522 HCMV encodes at least one other ER-resident immunevasin that activates the
523 UPR, US11 (56). UL148 binds the NK-cell and T-cell costimulatory ligand CD58 to
524 prevent its transport to the cell surface while US11 targets the heavy chain of class I
525 major histocompatibility complex (MHC) for ER-associated degradation (57, 58). UL148
526 causes CD58 to accumulate as an immature glycoform, presumably within the ER, but
527 does not lead to any obvious decrease in its overall abundance (9). Albeit that
528 intracellular forms of CD58 are in our hands refractory to detection by standard indirect
529 immunofluorescence protocols (data not shown), it seems reasonable to hypothesize
530 that UL148 sequesters CD58 into the unusual ER structures that it induces. Moreover,
531 our detergent solubility results suggest that UL148 may form aggregates or polymers in
532 the course of preventing CD58 presentation at the cell surface (FIG 8). It is worth
533 noting that UL148, an immunevasin targeting CD58, induces dramatic morphologic
534 rearrangements of the ER, while another HCMV immunevasin, US11, targeting MHC
535 class I for degradation evidently does not do so, even though both trigger ER stress.
536 Nonetheless, it seems unlikely that retention of CD58 would be required for ER

537 reorganization. In fact, the capacity of UL148 to retain CD58 may be functionally
538 separable from its peculiar effects on the morphology and organization of the ER.
539 Despite that the relationship between the mechanism for CD58 retention and the
540 formation of UL148-dependent ER structures remains unresolved, our findings may
541 suggest a mechanism to explain the influence of UL148 on the tropism of the virus for
542 epithelial cells. These effects, exemplified by a ~100-fold replication advantage of
543 *UL148*-null viruses during infection of epithelial cells, correlate with decreased
544 expression of glycoprotein O (gO), a viral envelope glycoprotein, both in virions and in
545 infected cells (1). We previously reported that gO behaves as a constitutive ERAD
546 substrate during infection and that immature, newly synthesized forms of gO show
547 enhanced stability in the presence of UL148 (8). Our findings herein show that UL148
548 causes large-scale sequestration of cellular factors important for ERAD, such as the ER
549 mannosidase EDEM1 and the E3 ubiquitin ligase SEL1L/Hrd1, into large membranous
550 structures. Moreover, the reticular ER, as indicated by the staining patterns of
551 antibodies specific for calreticulin, PDI, and the KDEL motif, appears to remain largely
552 intact following UL148-induced ER reorganization (FIG 3, 10). Since these
553 observations indicate that UL148 depletes ERAD factors from the ER during the
554 formation of the unusual structures, regions of ER not drawn into the structures might
555 be expected to offer a more permissive folding environment for polypeptides, such as
556 gO, which either fold slowly or inefficiently assemble into multiprotein complexes.
557 Based on these observations, one might hypothesize that UL148 alters ER
558 proteostasis by physically dislocating (or sequestering) key elements of the “mannose
559 removal time clock” system that marks poorly folding glycoproteins for destruction via

560 ERAD (59, 60). Because gO is both the defining subunit of the heterotrimeric gH/gL/gO
561 envelope glycoprotein complex that governs HCMV entry and cell tropism (5-7, 61, 62),
562 and a constitutive ERAD substrate (1, 8), ER reorganization might be required for the
563 effects of UL148 on HCMV cell tropism. Going forward, it will be crucial to determine
564 whether classical ERAD substrates, such as the null Hong Kong variant of alpha-1-
565 antitrypsin (63, 64) or ribophorin-332 (65, 66), are stabilized during UL148 expression,
566 as would be predicted if UL148 shifts ER proteostasis to negatively modulate ERAD.
567 In addition to having found that factors involved in proteasomal ERAD, such as
568 Hrd1 and EDEM1, are enriched at the UL148 structures, we observed that GABARAP,
569 a mammalian ortholog of yeast ATG8, localizes to the UL148 ER structures during
570 infection, and that another ATG8 ortholog, LC3B, and GABARAP both associate with
571 the structures during ectopic expression of UL148. This may suggest roles for
572 autophagy-related pathways in UL148-dependent reorganization of the organelle.
573 Since our results indicate that UL148 is degraded by a proteasome-dependent pathway
574 and not by lysosomes (**FIG S7**), it seems unlikely that selective autophagy of the ER is
575 directly involved in recycling or degrading these ER structures. Nonetheless, ATG8
576 family proteins may contribute to formation of the globular ER structures, since we
577 observed trafficking of UL148-GFP puncta to form large aggregates during live cell
578 imaging (**FIG 12, 15, Movies S2, S8**). The literature indicates that misfolded proteins
579 traffic in a microtubule (MT)-dependent manner to form pericentriolar structures termed
580 aggresomes, which in the case of ERAD substrates such as the ΔF508 mutant of the
581 cystic fibrosis transmembrane conductance regulator (CFTR), contain deglycosylated
582 protein that presumably has already undergone dislocation from the ER (67, 68). ATG8

583 family proteins such as LC3B and GABARAP not only play roles in degradation of
584 substrates via macroautophagy, but also bind MTs and recruit machinery for MT-
585 dependent transport of cargos (69-71). Therefore, GABARAP and LC3B may be
586 important for the recruitment of cellular machinery that transports perturbed ER cargoes
587 to sites of large-scale accumulation.

588 Although our results argue that the ISR is required for ER reorganization during
589 UL148 expression, precisely how UL148 triggers ER stress remains unknown. UL148
590 has been found to co-purify from cells with SEL1L, a component of the ERAD
591 machinery. Thus, it seems plausible that UL148 may inhibit the Hrd1/SEL1L complex,
592 which would cause the buildup of unfolded proteins and thus trigger the UPR. However,
593 inhibition of ERAD in and of itself seems unlikely to account for the formation of ER
594 structures. Another non-mutually exclusive possibility is that UL148 multimerizes or
595 aggregates in a manner that constricts the ER lumen. For instance, the assembly of
596 UL148 molecules on opposite sides of the ER lumen might constrict the organelle in a
597 manner consistent with the collapsed regions of ER observed in our EM results (**FIG 6,**
598 **8**).

599 Additional work will be needed to decipher the molecular mechanisms by which
600 UL148 causes reorganization of the ER, and to determine its physiological relevance in
601 the setting of viral biology. Nonetheless, we have shown that UL148, when fused to a
602 fluorescent protein (FP), suffices both to trigger and to indicate the presence of a
603 functional ISR (**FIG 10-11, S5**). Hence, UL148-FP fusions may prove useful in high
604 throughput chemical-genetic screens to identify novel small molecule inhibitors of the
605 ISR as well as to identify cellular genes involved in stress-dependent remodeling of the

606 ER. Interestingly, the two pharmacological agents that block UL148-dependent ER
607 remodeling, ISRIB and GSK2606414, are known to prevent the formation of stress
608 granules (SGs) (43, 72). SGs are comprised of condensed aggregates of protein and
609 RNA which occur due to stalled mRNA translation in the context of disease states, such
610 as amyotrophic lateral sclerosis (73), as well as during treatments with toxic agents
611 such as arsenite (43, 72). It is fascinating to consider that mechanistic parallels exist
612 between the formation of SGs and the UL148-dependent reorganization of the ER.
613 Moreover, given the broad importance macromolecular aggregation in pathological
614 conditions such as neurodegenerative diseases (74), certain of which also involve
615 defects in ER proteostasis and aberrant activation of the UPR, UL148 may hold promise
616 as tool to discover new agents to ameliorate disease.
617

618 **MATERIALS AND METHODS.**

619

620 **Cells and virus.**

621 hTERT-immortalized human foreskin fibroblasts (8), derived from ATCC HFF-1 cells
622 (SCRC-1041) were maintained in Dulbecco's modified Eagle's medium supplemented
623 with 5%-10% newborn calf serum (Millipore Sigma) and antibiotics (complete DMEM)
624 exactly as described previously (8). i148^{HA} and i159^{HA} ARPE-19 epithelial cells (10),
625 which upon treatment with 100 ng/mL doxycycline, express HA-tagged UL148 or
626 Rh159, respectively, were likewise maintained in complete DMEM. For live cell imaging
627 studies, i148^{HA} and i159^{HA} ARPE-19 were maintained in Opti-MEM (Thermo Fisher)
628 supplemented with 3% certified tet-approved fetal bovine serum (FBS), 20 µg/mL
629 gentamicin sulfate, 1 µg/mL puromycin HCl and 10 µg/mL ciprofloxacin HCl.
630 Telomerase-immortalized rhesus fibroblasts (75) were a kind gift of Peter A. Barry, and
631 were maintained in complete DMEM. The acute monocytic leukemia cell line THP-1
632 (TIB-202) was obtained from ATCC (Manassas, VA) and maintained as suspension
633 cultures in RPMI 1640 medium supplemented with 10% FBS (Millipore Sigma) and
634 antibiotics (10 µg/mL ciprofloxacin and 25 µg/mL gentamicin). THP-1 were
635 differentiated into adherent macrophages by incubating for 48 h in the presence of 100
636 nM 2-O-tetradecanoylphorbol 13-acetate (Millipore Sigma), and subsequently infected
637 with the indicated viruses at an MOI of 5 $TCID_{50}$/cell.

638 Infectious bacterial artificial chromosome (BAC) clones of the following HCMV
639 strains were used for this study: TB40/E (also known as TB40-BAC4 or TB_WT) (11)
640 as well as its derivatives TB_148^{HA} and TB_148$_{STOP}$, which were used in our previous

641 studies (1, 8, 10); TR (TR*gfp*) (76, 77); Merlin repaired for *UL128* and *RL13* harboring
642 *tetO* sequences upstream of *UL131* (pAL1393) (78); AD169 repaired for *UL131*
643 (AD_r131)(1, 79) and AD_r131_148^{HA}, a derivative of AD_r131 that carries a full length
644 UL148 (from strain TB40/E) tagged with an HA-epitope at the original *UL148* locus (8).
645 An infectious BAC clone of rhesus CMV (RhCMV) strain 68-1 (80) and a derivative that
646 expresses an HA-tagged Rh159 (details below) were also used for certain experiments.
647 The methods used for reconstitution of HCMV from purified BAC DNA, cultivation of
648 virus and preparation of stocks, including ultracentrifugation through sorbitol cushions
649 and determination of infectious titers by tissue culture infectious dose 50 ($TCID_{50}$) assay
650 have been described elsewhere (8, 10).
651
652 **Construction of recombinant viruses and new plasmids for the study.**
653 New recombinant viruses for this study were derived from BAC-cloned HCMV
654 and RhCMVs using *en passant* mutagenesis in GS1783 *E. coli,* a strain K12 derivative
655 that expresses the homing endonuclease I-SceI upon treatment with L-(+)-arabinose
656 (81, 82). Recombinant BACs were confirmed by Sanger DNA sequencing of the
657 modified regions, which was performed by Genewiz, Inc. (Piscataway, NJ) (not shown).
658 Oligonucleotide primers for construction of recombinant viruses and plasmids were
659 custom synthesized by Integrated DNA Technologies (Coralville, IA); sequences are
660 provided in **Table S1**. Type II restriction endonucleases, T4 DNA ligase, and Gibson
661 assembly reagents (NEB HiFi Assembly Master Mix) for generation of recombinant
662 DNAs and for routine molecular cloning and subcloning procedures were obtained from

663 New England Biolabs (Ipswitch, MA). KOD Hot Start DNA polymerase (EMD Millipore)
664 was used for all PCR reactions.
665 To construct TB_159^{HA}, a strain TB40/E derivative in which the UL148 open
666 reading frame is replaced by Rh159 we carried out the following steps. Primers
667 Rh159_Fw and Rh159_HA_Rv were used to amplify and HA-tag the *Rh159* ORF from
668 pcDNA3.1+_Rh159_IRES_GFP (a gift from Klaus Früh, OHSU). The PCR product was
669 inserted into EcoRV-digested pEF1α using Gibson assembly. A PCR product
670 containing an ISce-I excisable kanamycin cassette was amplified from TB_148^{HA}_*ISce-*
671 *Kan* integrate BAC (1) using primers PpuISceKanGibs_Fw and PpuISceKanGibs _Rv
672 and Gibson-assembled into PpuMI-digested pEF1α_Rh159 plasmid to yield plasmid
673 pEF1α_Rh159_ISceKan. Primers Rh159_Fw_recomb and Rh159_Rv_recomb were
674 used to generate a PCR product from template plasmid pEF1α_Rh159_ISceKan. The
675 PCR product was electroporated into GS1783 E. coli harboring the TB_148^{HA} BAC, and
676 Kan^r colonies harboring TB_Δ148_Rh159_ISceKan integrate BACs were isolated on
677 Luria-Bertiani agar plates. Bacterial colonies representing kanamycin resistant
678 integrates were obtained and were subsequently resolved to 'scarlessly' remove the
679 positive selection marker by standard *en passant* protocols (81, 82) to yield
680 TB_Δ148_Rh159^{HA}, which we abbreviate herein as TB_159^{HA}. TB_159^{HA} was
681 sequence-confirmed using primers TB_159HAseq_F and TB_159HAseq_R. Similar
682 strategies were used to modify the RhCMV 68-1 BAC (80) to incorporate sequences
683 encoding an HA-epitope immediately before the stop codon of *Rh159*. An *en passant*
684 strategy in which a shuttle plasmid carrying *I-SceI-Kan^r* disrupted by in-frame nonsense
685 codons was used insert premature nonsense codons in the *UL148* CDS in the context

686 of HCMV strains Merlin (pAL1393) and TR (TR*gfp*), and was applied as described
687 previously for generating TB_148$_{STOP}$, the UL148$_{STOP}$ mutant of strain TB40/E (8).
688 To construct "tet-on" lentivirus vector plasmids containing UL148 fused to GFP,
689 we used primers Gibs_eGFP_Rv and 148_eGFP_Fw to amplify the GFP gene from a
690 dsDNA gBlock, EGFP-P2A-3XHA, synthesized by Integrated DNA Technologies
691 (Coralville, IA), which was a gift of Matthew D. Woolard (LSU Health Sciences Center,
692 Shreveport, LA). In a separate PCR, the *UL148* gene was amplified from plasmid
693 pcDNA3.1-UL148^{HA} (10) using primers Gib_148_Fw and 148_noStopRv. The two
694 products were assembled, using Gibson Assembly, together with EcoRV opened
695 pcDNA3.1(+) (Invitrogen) to produce pcDNA3.1-UL148-GFP. After confirming the
696 absence of spurious mutations by Sanger DNA sequencing (Genewiz, not shown), the
697 *UL148-GFP* cassette from pcDNA3.1-UL148-GFP was released by EcoRI and NotI
698 digestion and ligated into pOUPc turboRFP-link plasmid which had been linearized
699 using the same restriction sites. pOUPc turboRFP-link is a derivative of lentiviral vector
700 pOUPc (10) that was constructed by reinsertion of turboRFP (tRFP). Briefly, tRFP was
701 amplified from the original pOUPc-turboRFP using primer pair tRFP linker Fw and tRFP
702 linker Rv and then reinserted by Gibson Assembly with pOUPc turboRFP that had been
703 double-digested using EcoRI and Not I in order to linearize the vector and remove the
704 *turboRFP* (RFP) sequence.
705 To express Rh159 fused to eGFP, primers Gibs_eGFP_Rv and 159_eGFP_Fw
706 were used to amplify the GFP gene from EGFP-P2A-3XHA, and in a separate PCR
707 reaction, primers Gibs_159_Fw and 159_noStop_Rv Rh159 were used to amplify
708 *Rh159* from pcDNA3.1-Rh159^{HA} (10). The latter two PCR products were assembled

709 together with EcoRV linearized pcDNA3.1(+) using Gibson Assembly, resulting in
710 plasmid pcDNA3.1-Rh159. The latter plasmid was used as template in a PCR reaction
711 with primers Gibs_Age_159_Fw and Gibs_Mlu_GFP_Rv. The resulting PCR product
712 was Gibson assembled into the lentiviral vector pOUPc (10) which had been double-
713 digested with Mlu I and Age I.
714
715 **Drug treatments.**
716 The PERK inhibitor, GSK2606414 (50), doxycycline hyclate, and folimycin were
717 obtained from MilliporeSigma (Burlington, MA). ISRIB (42-46) was obtained from
718 MilliporeSigma or APExBio (Boston, MA) and epoxomicin was procured Selleck
719 Chemicals (Houston, TX). ISRIB was dissolved in DMSO to make a 10,000× stock
720 solution (2 mM) and used at a final working concentration of 200 nM. GSK2606414 was
721 dissolved in DMSO to make a 10,000× stock solution (11 mM) and used at a final
722 working concentration of 1.1 μM. Folimycin was prepared as a 1000× (115.46 μM)
723 stock solution in DMSO and used at 115 nM final. Epoxomycin was prepared as a 100×
724 (2 mM) stock solution in DMSO and used at a final concentration of 20 μM.
725
726 **Confocal microscopy and live-cell imaging.** Confocal indirect immunofluorescence
727 microscopy imaging on fixed cells was carried out using Leica TCS SP5 Spectral
728 Confocal Microscope (Leica Microsystems, Heidelberg, Germany) using a Leica HCX
729 PL APO CS 63x/1.4-0.6NA objective under oil immersion, except for the image shown
730 in Figure 1C, which was captured on a Nikon SIM-E and A1R confocal microscopy
731 system (Nikon Instruments, Melville, NY) using a Nikon SR Apo TIRF 100x/1.49NA

732 objective under oil immersion. Images for different fluorophore channels were acquired
733 using sequential scanning. Direct immunofluorescence live cell imaging data were
734 collected using the Nikon SIM-E microscope using a Nikon Apo 60x/1.40NA DIC
735 objective. The 3D projection shown in FIG 1 was generated by NIS-Elements AR
736 Analysis 4.60.00 (64-bit) software (Nikon) from Z-stacks captured on the Nikon SIM-E /
737 A1R microscope using a Nikon SR Apo TIRF 100x/1.49NA objective. For FIG 11, 3D
738 projections were generated by Imaris x64 9.3.0 software (Bitplane, Inc.) in maximum
739 intensity projection (MIP) mode.

740 For fixed cell imaging experiments other than those shown in Fig S1D, cells were
741 seeded on 12 mm circular, No. 1 thickness microscope cover glass (200121; Azer
742 Scientific, Morgantown, PA). At the indicated times post-treatment and or post-infection,
743 cells were washed with phosphate buffered saline (PBS) [137 mM NaCl, 2.7 mM KCl, 10
744 mM Na_2HPO_4, and 1.8 mM KH_2PO_4, pH 7.4]; fixed for 15 min at room temperature in PBS
745 containing 4% (wt/vol) paraformaldehyde (Fisher Scientific, Waltham, MA), washed in
746 PBS, permeabilized for 10 min using 0.1% Triton X-100 (in PBS), subsequently washed
747 again in PBS, and then blocked for 45 min at 37 °C in PBS containing 5% (vol/vol) normal
748 goat serum (Rockland Immunochemicals, Limerick, PA). Cells were then washed three
749 times in PBS followed by incubation in 1% Human Fc Block (BD Biosciences, San Jose,
750 CA) in PBS, for additional 45 min at 37 °C. Cells were then incubated in the presence of
751 primary antibodies for 1 h at 37 °C or 4 °C overnight, and then washed three times with
752 PBS containing 0.1% Tween-20 (PBST) for 5 min per wash. Alexa Fluor-labeled goat
753 polyclonal secondary antibodies (all from ThermoFisher Invitrogen, Waltham, MA, see
754 **Table S2**) were used for secondary detection. The slides were then mounted using

755 Prolong Gold anti-fade reagent containing DAPI (ThermoFisher) and placed under a
756 Leica TCS SP5 confocal microscope for image acquisition using a Leica 63× oil
757 immersion objective lens (Leica Microsystems, Buffalo Grove, IL).

758 For indirect immunofluorescence staining results of primary clinical isolates (SI Fig
759 S1D), four clinical HCMV isolates obtained by routine testing of throat swabs from patients
760 of the Ulm University Medical Center were provided by the diagnostic laboratory of the
761 Institute of Virology in Ulm. Sample material was applied to human fibroblasts and
762 incubated for several days until HCMV-positive cells could be detected. Infected cells
763 were then seeded together with uninfected fibroblasts, incubated for up to 5 days until
764 plaques were formed and processed for indirect immunofluorescence staining. ERQC
765 compartments were detected by staining for calnexin (CNX, E10; Santa Cruz
766 Biotechnology, mouse, 1:50 dilution), the cVAC was detected by staining for HCMV
767 pUL71 (rabbit, 1:500). Secondary antibody used for detection of CNX was Alexa Fluor
768 555 labeled goat anti-mouse IgG (1:1000) and for pUL71 detection, Alexa Fluor 488
769 conjugated goat anti-rabbit IgG (1:1000). Confocal images were acquired using the 63×
770 objective of a Zeiss Observer Z1 fluorescence microscope equipped with Apotome and
771 Zen software 2.3 (Carl Zeiss Microscopy GmbH, Jena, Germany).

772

773 **FRAP.** FRAP studies were carried out on using live ARPE-19 cells from the i148^{GFP}
774 and i159^{GFP} populations as follows. Cells were seeded as above for live-cell imaging,
775 induced for transgene expression using dox (100 ng) for 24 h, and then placed on an
776 incubated sample stage of a Nikon A1R SIM-E imaging system equipped with an SR
777 Apo TIRF 100x/1.49NA objective (Nikon). Three rectangular regions in image fields

778 were defined for measurement of (i) background signal, and of two regions with
779 comparable initial GFP signals, (ii) one designated as a control region (no
780 photobleaching) and another for (iii) photobleaching and recovery of signal after
781 photobleaching. Photobleaching of selected regions was carried out for 20 s using 405
782 nm laser light from a LU-N4 laser fiber (Nikon) [power at source: 15 mW, power at
783 objective: 8 mW]. Images and signal intensity measurements were captured every 2 s
784 at a rate of 1 frame per s (488 nm excitation, FITC channel) starting immediately before
785 photobleaching (t=1), and from t=20 s to t=320 s after.
786
787 **Electron microscopy.** Procedures to prepare samples for transmission electron
788 microscopy (TEM) included high-pressure freezing (HPF), freeze substitution, and Epon
789 embedding, which were carried out as described previously (83). Briefly, human
790 fibroblasts were seeded in μ-Slides (Ibidi GmbH, Martinsried, Germany) containing
791 carbon-coated sapphire discs (Engineering Office M. Wohlwend GmbH) 1 day prior to
792 infection at 80 to 90% confluence. Cells were infected with virus overnight at MOI 1.
793 Medium containing viral inocula was replaced with fresh medium the next day. Infected
794 cells on sapphire discs were fixed by using HPF with a Compact 01 high-pressure freezer
795 (Engineering Office M. Wohlwend GmbH, Sennwald, Switzerland) at 5 dpi. Thereafter,
796 cells on sapphire discs were processed by freeze-substitution and subsequently
797 embedded in Epon (Fluka, Buchs, Switzerland). Ultrathin sections of the Epon-embedded
798 cells were cut with an ultramicrotome (Ultracut UCT; Leica Microsystems, Wetzlar,
799 Germany) and placed on Formvar-coated single-slot grids (Plano GmbH, Wetzlar,
800 Germany). Grids were examined in a Jeol JEM-1400 (Jeol Ltd., Tokyo, Japan)

801 transmission electron microscope equipped with a charge-coupled-device (CCD) camera
802 at an acceleration voltage of 120 kV. Fixation and embedding of infected cells for
803 scanning transmission electron microscopy (STEM) tomography was the same as
804 described for TEM. Additional sample preparation steps were conducted as described
805 previously (84, 85). Tomogram acquisition was conducted on a STEM Jeol JEM-2100F
806 with an acceleration voltage of 200 kV. Tilt series were acquired from 600 nm thin
807 sections from +72° to -72° with a 1.5° increment using the bright field detector. Image
808 series were reconstructed to tomograms by weighted back projection with the IMOD
809 software package (86). 3D visualization of the membrane structures was performed using
810 Avizo lite software (Visualization Science Group, Burlington, MA, USA) by threshold
811 segmentation.
812
813 **Western blotting.** Western blotting procedures, including primary and secondary
814 antibodies used for detection of HA tag, UL148, ATF4, eIF2α, P-eIF2α (Ser51), the
815 HCMV viral nuclear antigen IE1, and the conditions used for detection of Ser51
816 phosphorylated eIF2α, were carried out as described previously (8, 10). Additional
817 antibodies used in this study were mouse anti-GAPDH (Cat. No. 60004-1, Proteintech,
818 Rosemont, IL,), mouse anti-gB clone 27-180 (87) (a generous gift of William J. Britt),
819 and anti-GFP (D5.1) XP® Rabbit mAb #2956 (Cell Signaling Technology, Danvers, MA).
820
821 **Solubility analyses.** 2.0×10^5 human fibroblasts were infected at an MOI of 1 $TCID_{50}$
822 per cell with TB_148^{HA} or TB_159^{HA}. The following day, cells were washed twice with
823 PBS to remove viral inoculum and replenished with DMEM containing 5% newborn calf

824 serum. At the indicated times post-infection, cells were washed once with PBS and
825 lysed by direct addition of 100 μL RIPA buffer [25 mM HEPES (pH 7.5), 400 mM NaCl,
826 0.1% SDS, 0.5% sodium deoxycholate, 1% NP-40, supplemented with 1× protease
827 inhibitor cocktail (ApexBio)]. Lysates were collected and rotated at 4˚C for 1 h.
828 Insoluble material was pelleted by centrifugation (21,000 × *g*, 35 min). Supernatants
829 containing soluble material were transferred to a fresh microfuge tube, and 33 μL of 4×
830 Laemmli sample buffer [200 mM Tris (pH 6.8), 8% SDS, 40% glycerol, 0.08%
831 bromophenol blue] was added to bring final volume to 133 μL. The pellet was disrupted
832 in 133 μL of 1X Laemmli buffer prepared by diluting 4× Laemmli buffer in RIPA buffer.
833 Samples were reduced by addition of beta-mercaptoethanol (5% final, v/v) and boiled at
834 90˚C for 10 min. 40 μL of each sample was resolved by SDS-PAGE (12%
835 polyacrylamide gel), transferred overnight to nitrocellulose membrane, and
836 immunoblotted with antibodies against HA epitope or HCMV gB. Quantitation of
837 secondary antibody fluorescence signals were performed using an Odyssey CLx
838 scanner (Li-Cor, Inc., Lincoln, NE) in auto-scan mode. For each time-point, the signals
839 from RIPA-soluble and insoluble bands were summed to yield total signal, and the ratio
840 of insoluble band signal to total signal were also reported as percent insoluble HA over
841 total HA signal.
842
843 **Statistical analyses.** Statistical analyses were carried out using GraphPad Prism 8.1.0
844 for MacOS (GraphPad, Inc., San Diego, CA).
845
846 **ACKNOWLEDGEMENTS.**

847 This project was supported by NIH grants R01-AI116851 (to J.P.K.) and P30-
848 GM110703. Its contents are solely the responsibility of the authors and do not
849 necessarily represent the official views of the NIAID or the NIGMS.
850 We are especially grateful to Erik L. Snapp (HHMI, Janelia Laboratories) for
851 helpful discussions and detailed advice on interpretation of EM and confocal image
852 data. We also thank Dong Yu (Washington University, St. Louis, MO, currently GSK
853 Vaccines), Thomas E. Shenk (Princeton University, Princeton, NJ), Richard J. Stanton
854 (Cardiff University, United Kingdom), William J. Britt (University of Alabama,
855 Birmingham), W. L. William Chang and Peter A. Barry (both of the University of
856 California, Davis; Davis, CA), Christian Sinzger (University Medical Center Ulm, Ulm,
857 Germany), Klaus Früh (Oregon Health Sciences University, Beaverton, OR), and
858 Gregory A. Smith (Northwestern University, Chicago, IL) for generously sharing
859 reagents.
860

861 **AUTHOR CONTRIBUTIONS.**

862 Performed experiments: HZ, CR, CCN, MNAS, JvE. Data analysis and interpretation:
863 HZ, CR, CCN, JvE, CS, JPK. Designed experiments: HZ, CR, CCN, JvE, and JPK.
864 Contributed new reagents: HZ, CH, CCN, JPK. Electron microscopy and STEM
865 tomography: CR and JvE. Obtained funding: JPK. Wrote the manuscript: JPK with
866 comments from JvE and CR.

867 **FIGURES**

868

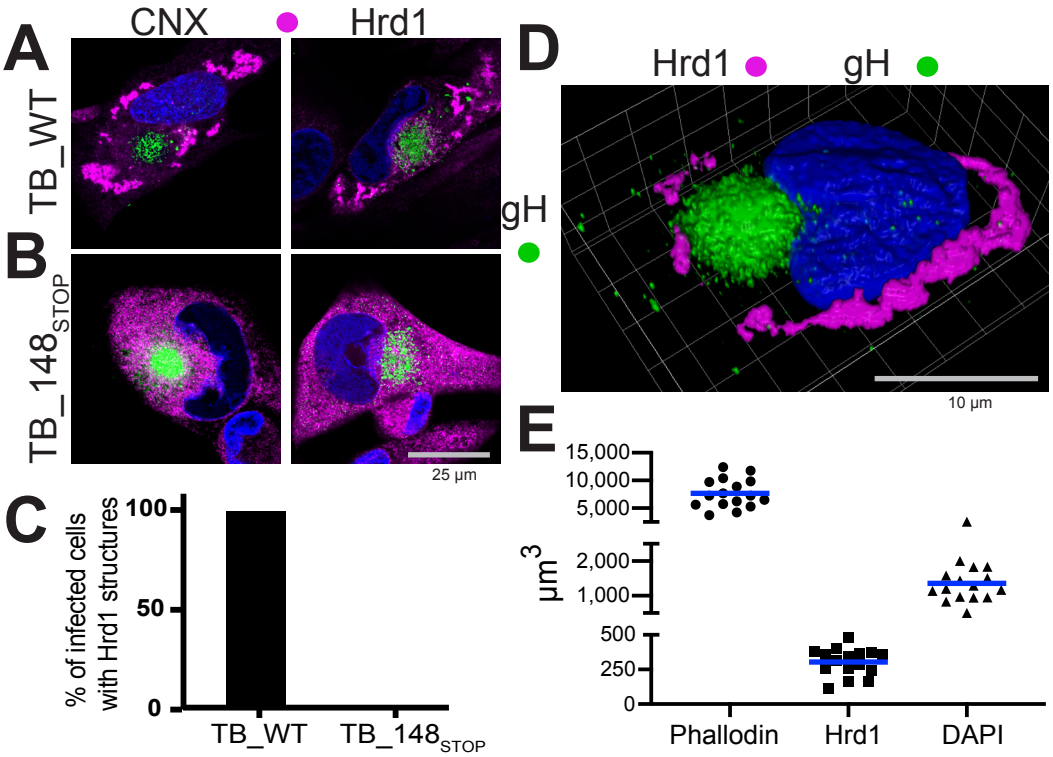

869
870

871 **FIG 1. UL148 reorganizes ER markers into anomalous structures during HCMV infection.**
872 Fibroblasts infected at 1 MOI with either **(A)** wildtype HCMV strain TB40/E (TB_WT) or **(B)** an
873 isogenic *UL148*-null mutant (TB_148$_{STOP}$), were fixed at 96 h postinfection (hpi) and imaged by
874 confocal microscopy after staining with antibodies specific for calnexin or Hrd1 (magenta) and
875 glycoprotein H (gH, green), as indicated. DAPI (blue) signal was used to counterstain nuclei. **(C)**
876 Percentage of fibroblasts that contain Hrd1 structures at 96 hpi; fifty gH-positive cells for each
877 condition were scored for the presence or absence of UL148 structures (also see SI Fig S1A).
878 (**D**) 3D confocal image projection of a TB_WT infected fibroblast stained at 96 hpi for Hrd1 and
879 gH. **(E)** Volumetric measurements were made from sixteen infected cells, stained with phalloidin-
880 AlexaFluor 594 conjugate to estimate total cell volume, with Hrd1 antibody to estimate the volume
881 of UL148-dependent ER structures, and with DAPI to estimate nuclear volume.
882
883
884
885
886

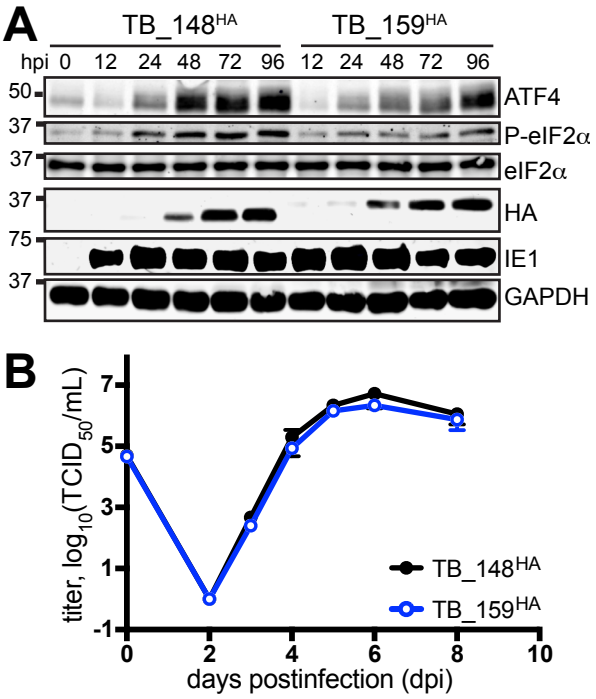

FIG 2. Characterization of TB_148^{HA} and TB_159^{HA} viruses. (A) Human fibroblasts were infected at MOI 1 with the indicated recombinant HCMVs. Cell lysate samples harvested at the indicated times postinfection (h postinfection, hpi) were analyzed by Western blot to detect HA-tagged UL148 or Rh159, the 72 kD viral nuclear antigen IE1-72 (IE1), and GAPDH. **(B)** Single-cycle viral replication kinetic curves from MOI 1 infected fibroblasts were plotted by determining the titer in tissue culture infectious dose 50 ($TCID_{50}$) from supernatants collected at the indicated times postinfection.

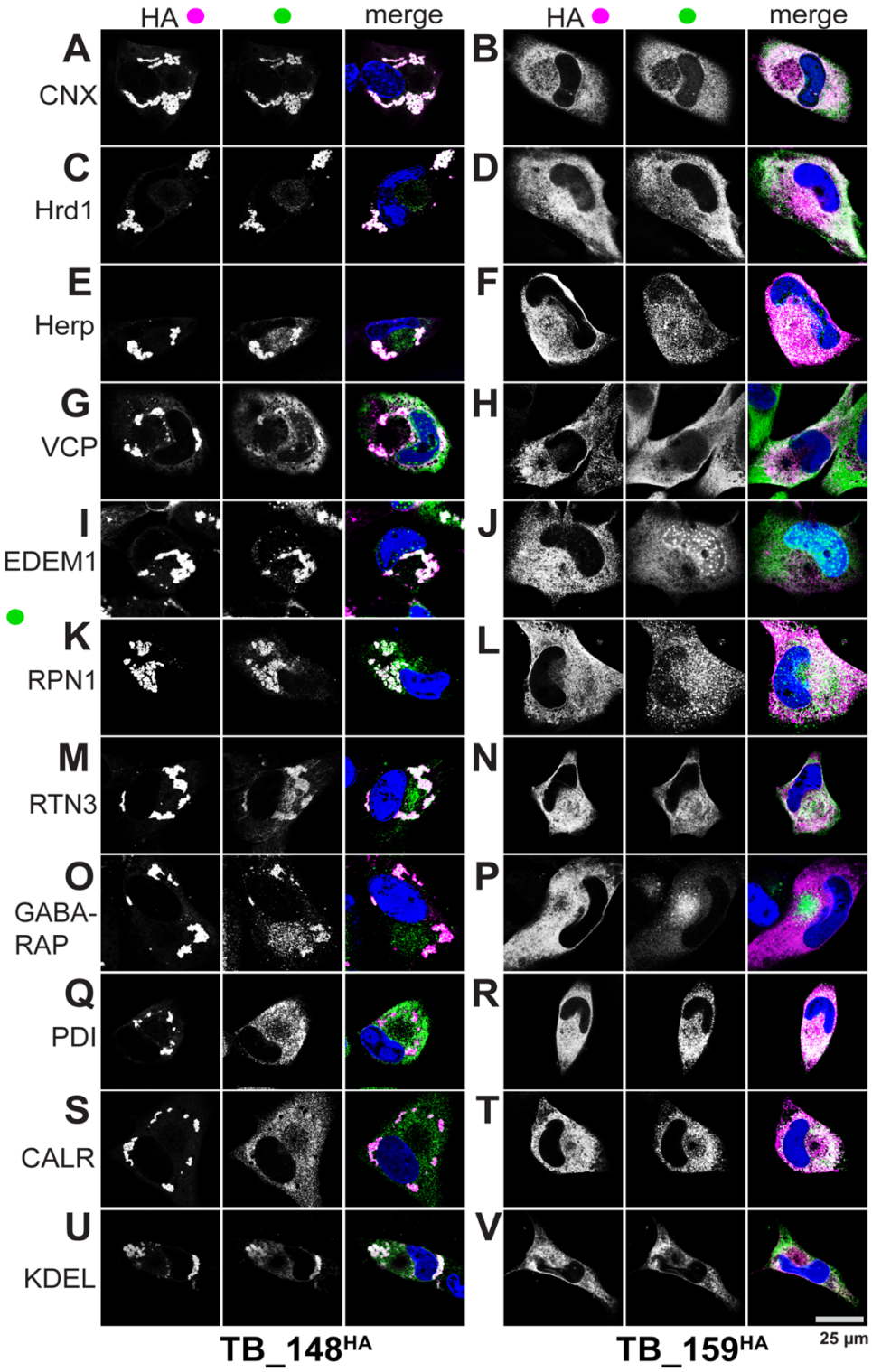

FIG 3. UL148 localizes to unusual ER compartments that are enriched for glycoprotein quality control markers. Fibroblasts infected at MOI 1 with either TB_148^{HA} (panels: **A, C, E, G, I, K, M, O, Q, S**) or TB_ 159^{HA} (panels: **B, D, F, H, J, L, N, P, R, T**) were fixed at 96 h postinfection, and imaged by confocal microscopy after co-staining with antibodies specific for HA (UL148 / Rh159, magenta in merge) and the indicated cellular markers (green in merge). DAPI (blue) counterstaining is shown in merged image.

903
904
905

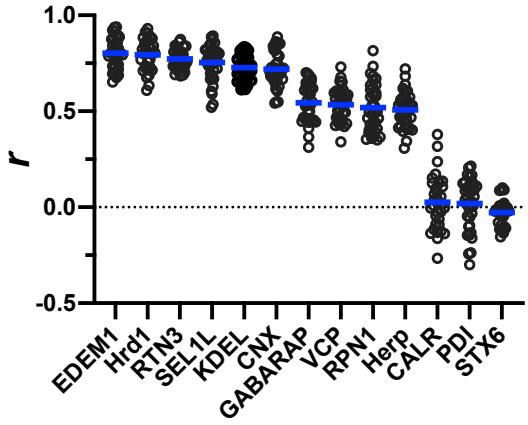

906
907 **FIG 4. Quantification of co-localization between UL148 and cellular markers.** A Pearson's
908 correlation coefficient (*r*) was calculated using NIH ImageJ software to estimate the degree of co-
909 localization between UL148 (HA signal) and each of the indicated cellular markers. A minimum
910 of 30 cells were analyzed per marker. The arithmetic mean for each co-localization analysis result
911 is shown as a blue line, and data points for individual cells analyzed are plotted as circles.
912

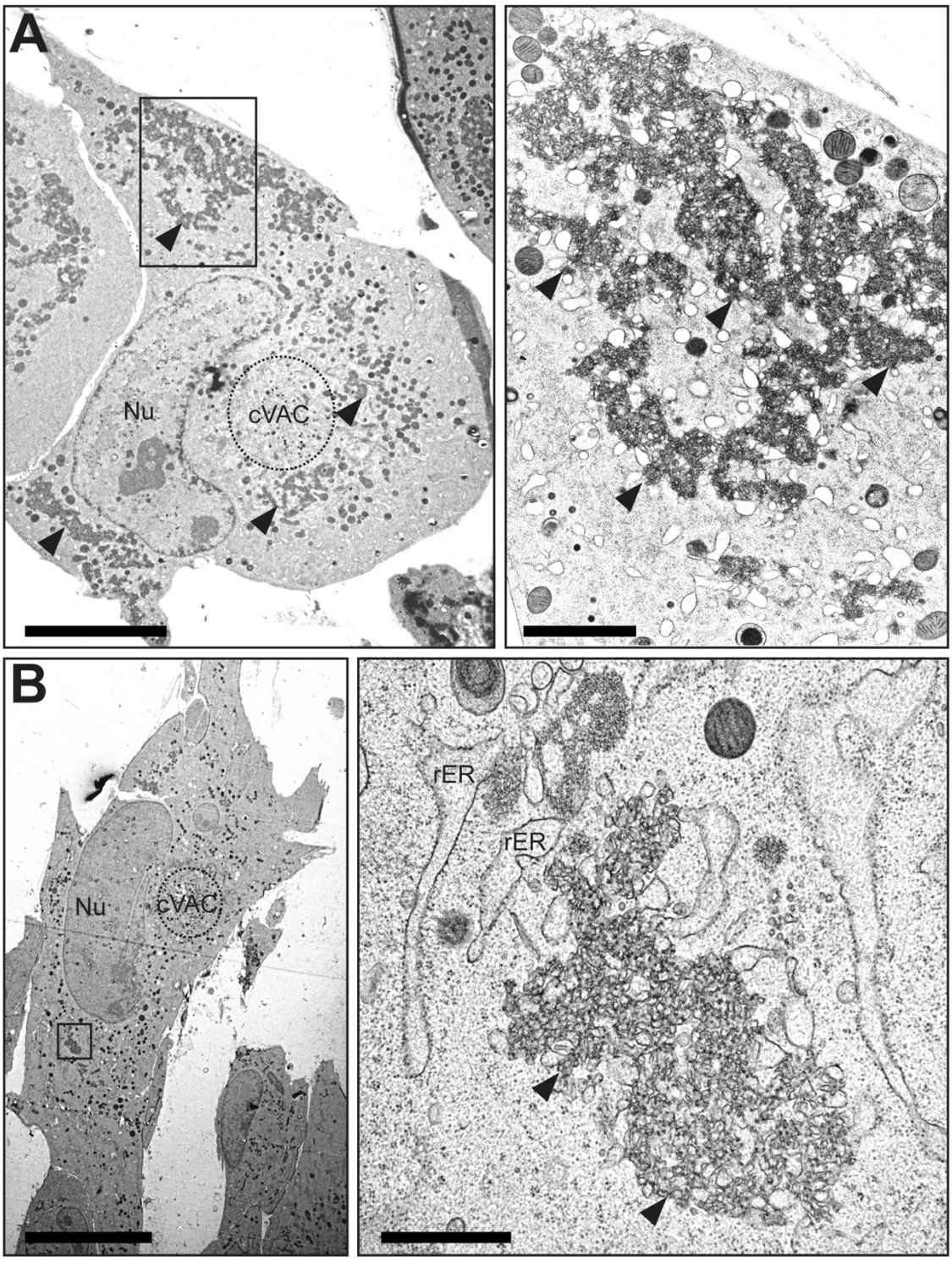

FIG 5. TEM of ER structures in wild-type HCMV infected cells. Human fibroblasts infected with wildtype HCMV (TB_WT) were fixed by high-pressure freezing and freeze substitution at day 5 postinfection and imaged using TEM. Panels (**A**) and (**B**) show cell overview at left. For each cell, the boxed region is shown at higher magnification. Scale bars; left panels: 10 µm, right panels: 2 µm. rER: rough ER; Nu: nucleus; cVAC: cytoplasmic viral assembly compartment. Solid arrowheads indicate the UL148-dependent ER structures of interest.

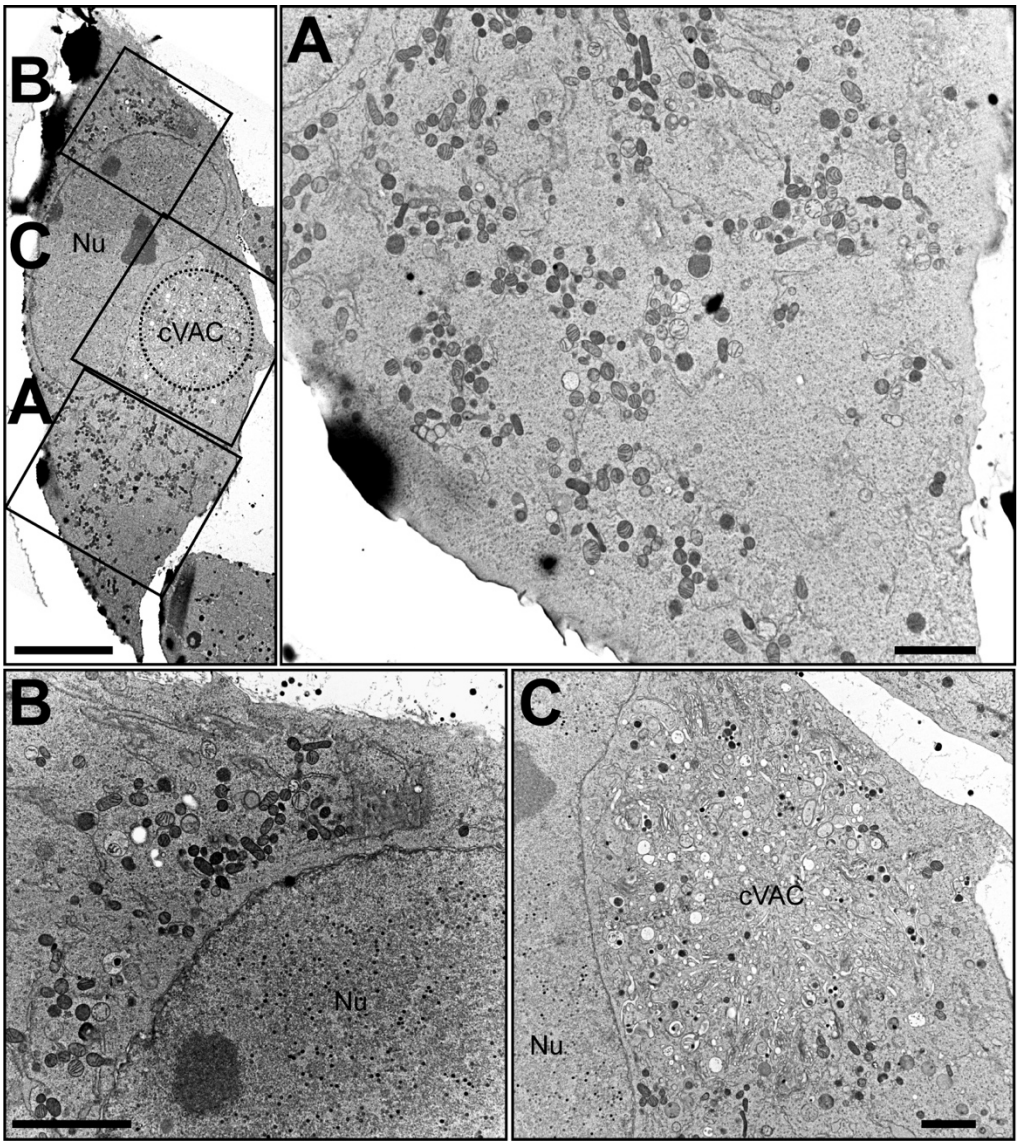

FIG 6. TEM of *UL148*-null HCMV infected cells. Human fibroblasts infected with a *UL148*-null mutant (TB_148$_{STOP}$) were fixed by high-pressure freezing and freeze substitution at day 5 postinfection and imaged using TEM. At the upper left an overview panel of a representative cell is shown with panels (**A)**, **(B)**, and **(C)** each boxed. The boxed regions are expanded at higher magnification at right (**A**) and below (**B, C**). Scale bars for upper left overview panel: 10 µm, for zoomed panels: 2 µm. rER: rough ER; Nu: nucleus; cVAC: cytoplasmic viral assembly compartment.

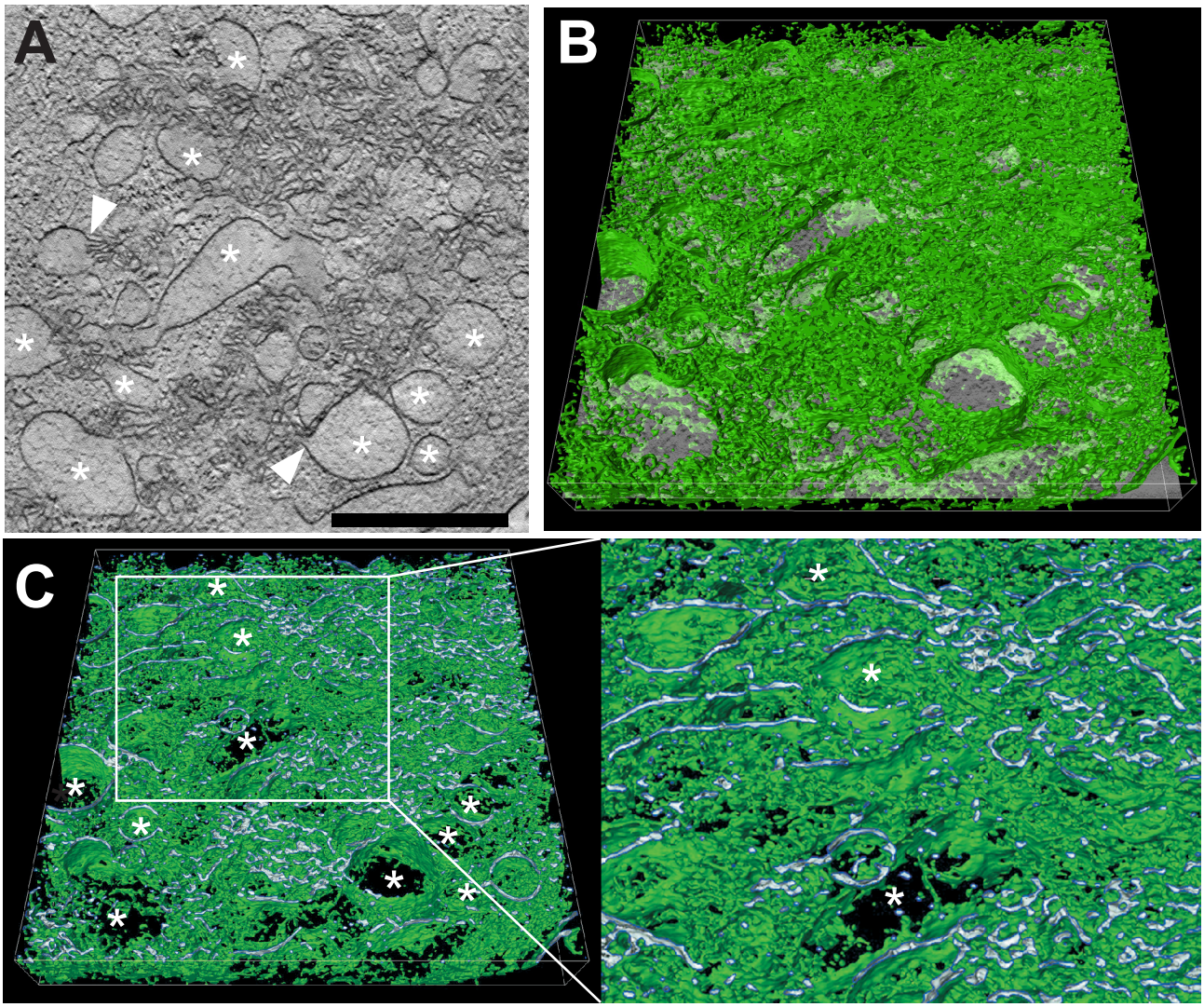

FIG 7. STEM tomography of UL148-dependent ER structures in HCMV infected cells. Human fibroblasts infected with wildtype HCMV (TB_WT) were fixed by high-pressure freezing and freeze substitution at day 5 postinfection and tomograms were recorded by STEM. (**A**) Shows a virtual section through the tomogram of a virus-induced membranous structure; asterisks denote ER structures of distended lumenal space. White arrowheads indicate sites at which membranes originating from distended ER cisternae continue into areas of involuted collapsed ER. Scale bar: 1 µm. (**B**) Shows the same virtual section as in (A) tilted and with a 3D visualization of the membranous network (green) of the entire tomogram. The same distended ER cisternae as in (A) are marked by asterisks. (**C**) Shows a cross section through (B) to visualize the membrane profile of the membranous structures. The region delimited by a white box is shown in a higher magnification on the right. Finer detail of the enlarged ER cisternae and the connections between them are readily visible; asterisks indicate the same distended ER cisternae as in panels (A) and (B). Also, see SI Movie S1. Scale bar: 1 µm.

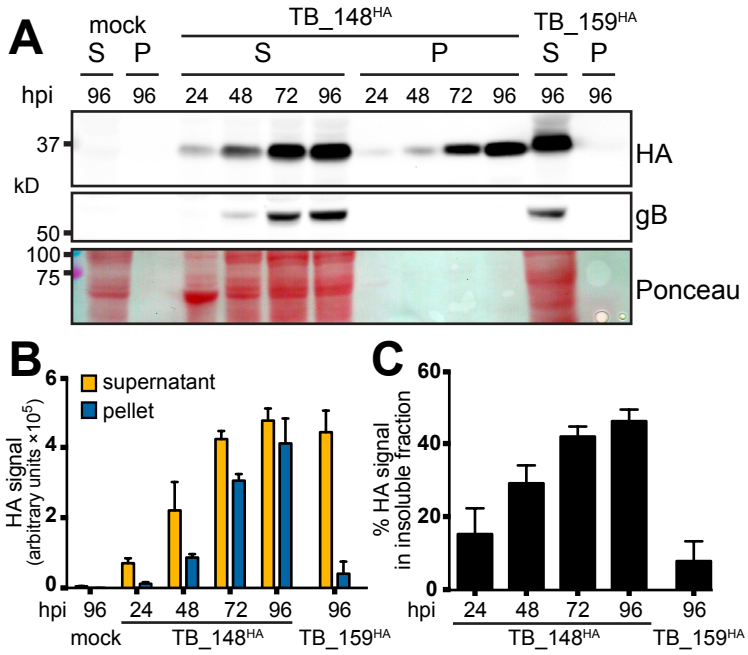

FIG 8. Solubility analysis of UL148 and Rh159. (**A**) Human fibroblasts were infected at MOI 1 $TCID_{50}$/cell with HCMV strain TB40/E derived viruses TB_148^{HA}, which expresses UL148 fused at its C-terminus to an HA-epitope tag, or TB_159^{HA}, which lacks *UL148* and instead expresses rhesus CMV Rh159 carrying a C-terminal HA tag. At the indicated times postinfection (hpi), infected cells were collected in radioimmunoprecipitation (RIPA) lysis buffer, centrifuged at 21,000 × *g* for 30 min, after which supernatant (S) and pellet (P) fractions were boiled in gel loading buffer containing 2% sodium dodecyl sulfate (SDS). Equivalent portions of supernatant and pellet were resolved by SDS-polyacrylamide gel electrophoresis, transferred to a nitrocellulose membrane for detection of protein species immunoreactive to antibodies against HA epitope (HA) and HCMV glycoprotein B (gB) and for total protein signal using Ponceau S reagent (Ponceau). (**B-C**). Signal intensity of fluorophore-conjugated secondary antibodies in anti-HA Western blots were measured from three independent biological replicates of the experiment shown in (A); error bars indicate standard deviation. (**B**) The fluorescent signal for each infection time point condition (y-axis is in arbitrary units, in hundred thousands). (**C**) The amount of signal found in the insoluble (pellet) fraction relative to the total signal (pellet plus supernatant) for each infection time point are plotted as percentage values.

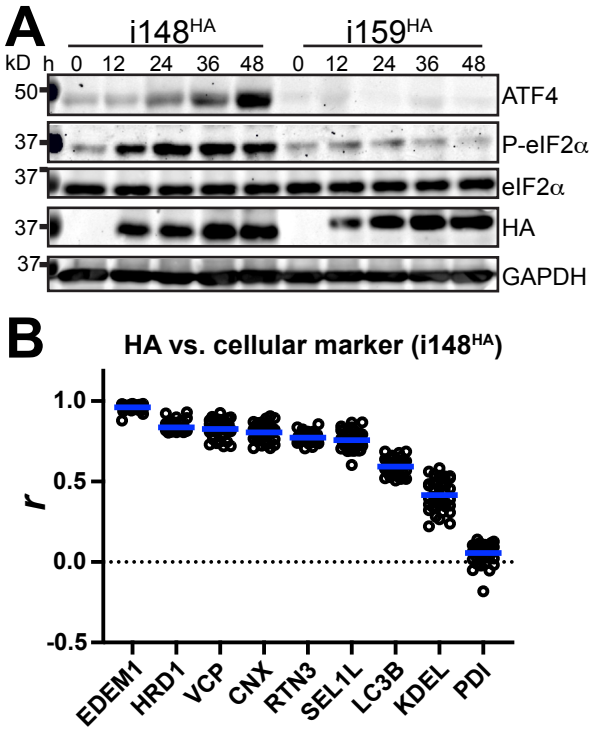

FIG 9. ISR activation accompanies redistribution of ER markers during ectopic expression of UL148. (A) Lysates of tet-on ARPE-19 cells expressing either UL148 or Rh159 fused to an HA tag, i148^{HA} and i159^{HA}, respectively, were collected at the indicated times post doxycycline (dox) induction and analyzed by Western blot for the expression of the indicated proteins and for the abundance of eIF2α phosphorylated at Ser51 (P-eIF2α) using a phospho-specific antibody. (**B**) Pearson's correlation coefficient (*r*) values were calculated using NIH ImageJ software estimate the degree of co-localization between UL148 (HA signal) and the indicated cellular markers. A minimum of 30 cells were analyzed per marker. Arithmetic means for each co-localization analysis result are shown as blue lines, and data points for individual cells analyzed are plotted as circles.

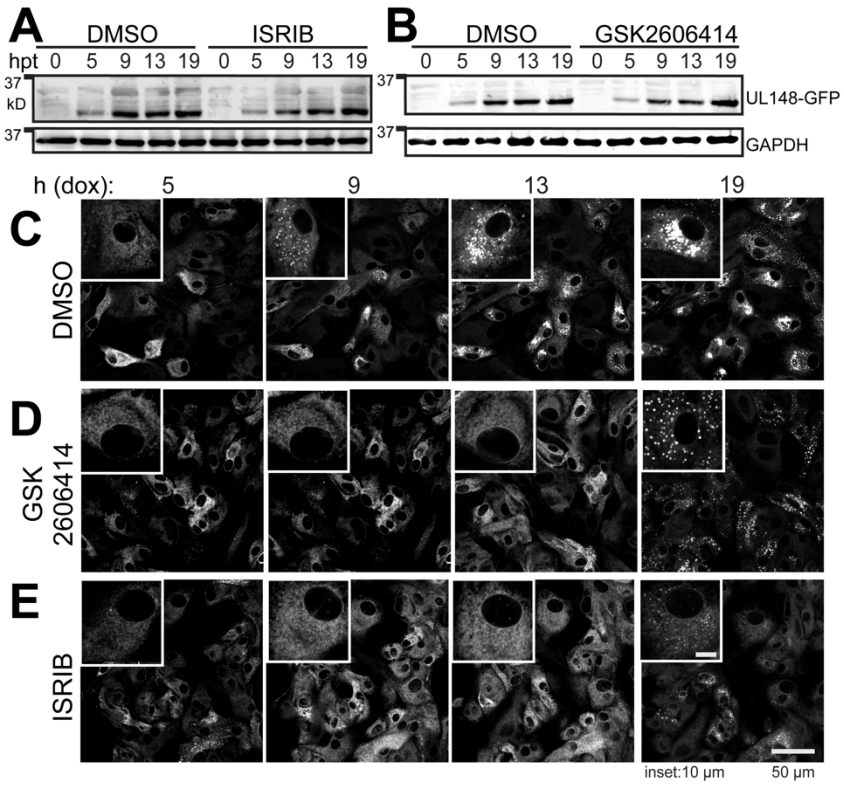

FIG 10. Inhibition of the integrated stress response impedes UL148-mediated ER remodeling. (A-B) "Tet-on" ARPE-19 epithelial cells that inducibly express UL148 fused to green florescent protein (gfp), i148^{gfp}, were induced for transgene expression using 100 ng/mL doxycycline (dox) in the presence of DMSO carrier, ISRIB (200 nM), or GSK2606414 (1.1 µM) and monitored by anti-UL148 Western blot for expression of UL148-GFP over a series of time points (h post treatment with dox, hpt). (**C-E**) Live-cell imaging of UL148-GFP expression patterns in the presence of ISRIB (200 nM), GSK2606414 (1.1 µM), or DMSO vehicle (0.01%). Main scale bar represents 50 µm. For inset panels at upper left of each image, which are magnified 2.4× relative to the main image, the scale bar represents 10 µm. Also see SI Movies S8-S10.

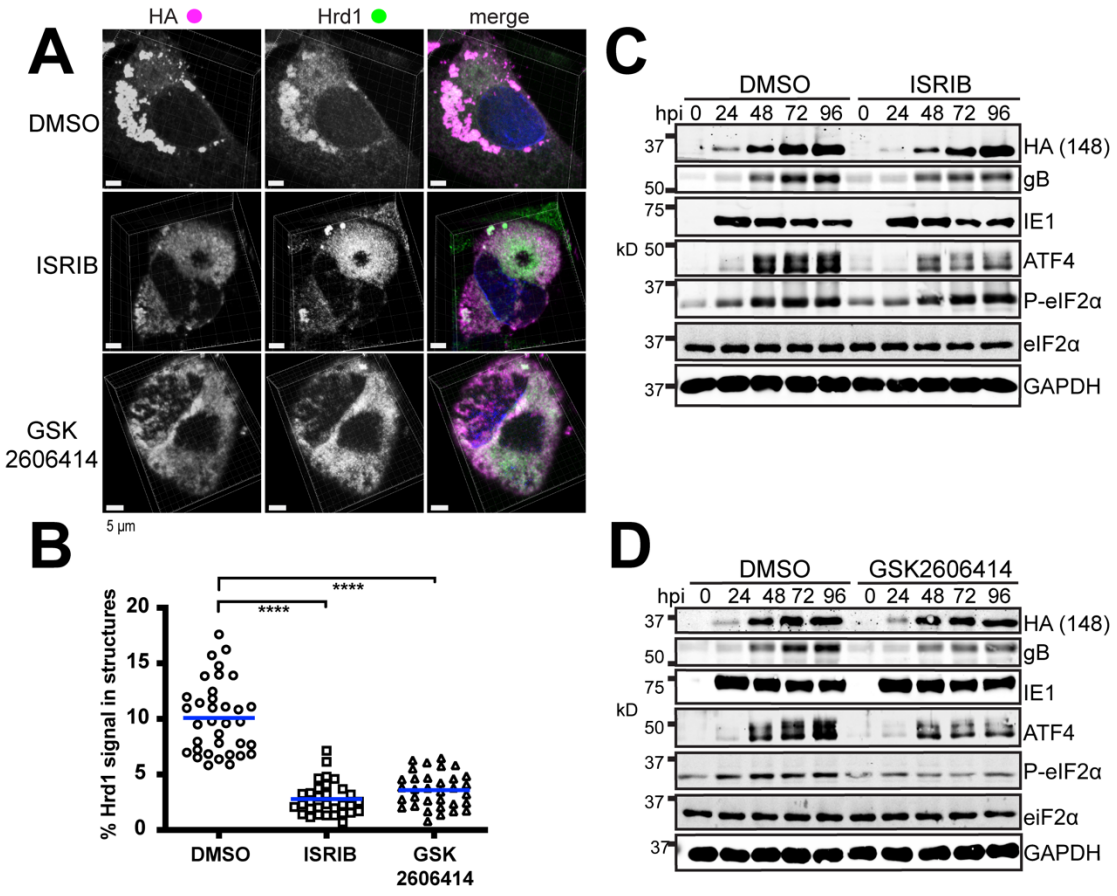

FIG 11. Inhibition of the ISR prevents the coalescence of Hrd1 and UL148 into discrete structures during infection. (**A**) Representative 3D maximum intensity projections of confocal imaging Z-stacks obtained from cells infected at MOI 1 for 96 h with HCMV strain TB40/E carrying an HA-tagged *UL148*, TB_148^{HA}, and maintained in the presence of ISRIB (200 nM), GSK2606414 (1.1 µM), or DMSO carrier alone (0.1% vol/vol). In merged images HA signal is shown in magenta, Hrd1 in green, and DAPI counterstaining in blue. (**B**) The percent of Hrd1 antibody signal involved in discrete structures at 96 hpi were calculated for a minimum of 30 cells per condition using Imaris x64 9.3.0 software. Statistical significance was determined using a one-way ANOVA followed by Tukey's post-test; **** represents a P-value of <0.0001. The arithmetic mean for co-localization analysis results are shown as blue lines with data points for individual cells analyzed plotted as circles, squares or triangles, as indicated. (**C-D**) Western blot analyses of fibroblasts infected at MOI 1 with TB_148^{HA} and maintained in the presence of ISRIB (200 nM), GSK2606414 (1.1 µM), or DMSO carrier alone (0.01%); hpi: h post infection (hpi). Note: a phospho-specific antibody was used for detection of eIF2α phosphorylated at Ser51 (P-eIF2α).

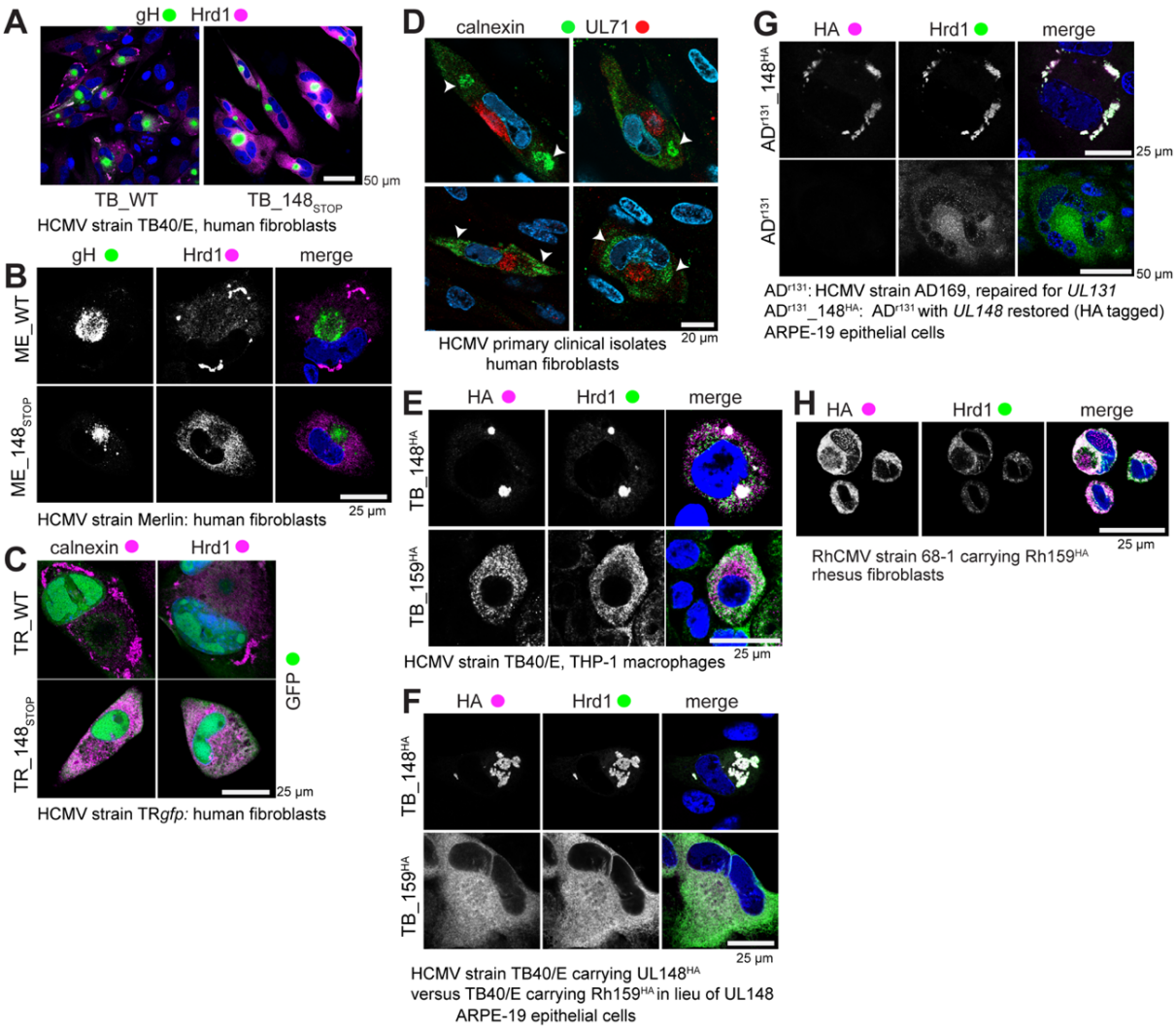

FIG S1: **Additional confocal microscopy results from infected cells.** (**A**) Lower magnification view of results from FIG 1; staining of gH and Hrd1 at 96 hpi of human fibroblasts with wildtype HCMV strain TB40/E (WT) versus *UL148*-null derivative TB_148$_{STOP}$. (**B**) gH and Hrd1 at 96 hpi of human fibroblasts with wildtype HCMV strain Merlin (ME_WT) or a *UL148*-null derivative of the same virus (ME_148$_{STOP}$). (**C**): gH and Hrd1 at 96 hpi of human fibroblasts with wildtype HCMV strain TRgfp recovered from BAC-cloned TRgfp (TR_WT) or a *UL148*-null derivative of the same virus (TR_148$_{STOP}$). (**D**) Staining of the viral tegument protein UL71 and calnexin of human fibroblasts infected with primary clinical HCMV isolates obtained from patient throat swabs (at 5 dpi). (**E**) HA and Hrd1 in THP-1 macrophages (differentiated using phorbol ester treatment) fixed at 96 hpi with HCMV strain TB40/E derivative viruses TB_148^{HA} or TB_159^{HA}. (**F**) HA and Hrd1 in ARPE-19 epithelial cells infected for 96 h with either TB_148^{HA} or TB_159^{HA}. (**G**) HA and Hrd1 in ARPE-19 infected for 96 h with HCMV strain AD169 repaired for *UL131* and to which an HA-tagged *UL148* from TB40/E was restored to the native *UL148* locus (AD^{r131}_148^{HA}) vs parental AD169 repaired for *UL131* (AD^{r131}). For ADr131 we did not employ a viral marker (e.g., HA) to identify infected cells, so the appearance of syncytia and the characteristic kidney-bean shaped nucleus was used to indicate infected cells, and a slightly lower magnification was used to best show these features. (**H**) HA and Hrd1 in telomerase-immortalized rhesus fibroblasts infected with RhCMV strain 68-1 carrying an HA-tag at the C-terminus of Rh159.

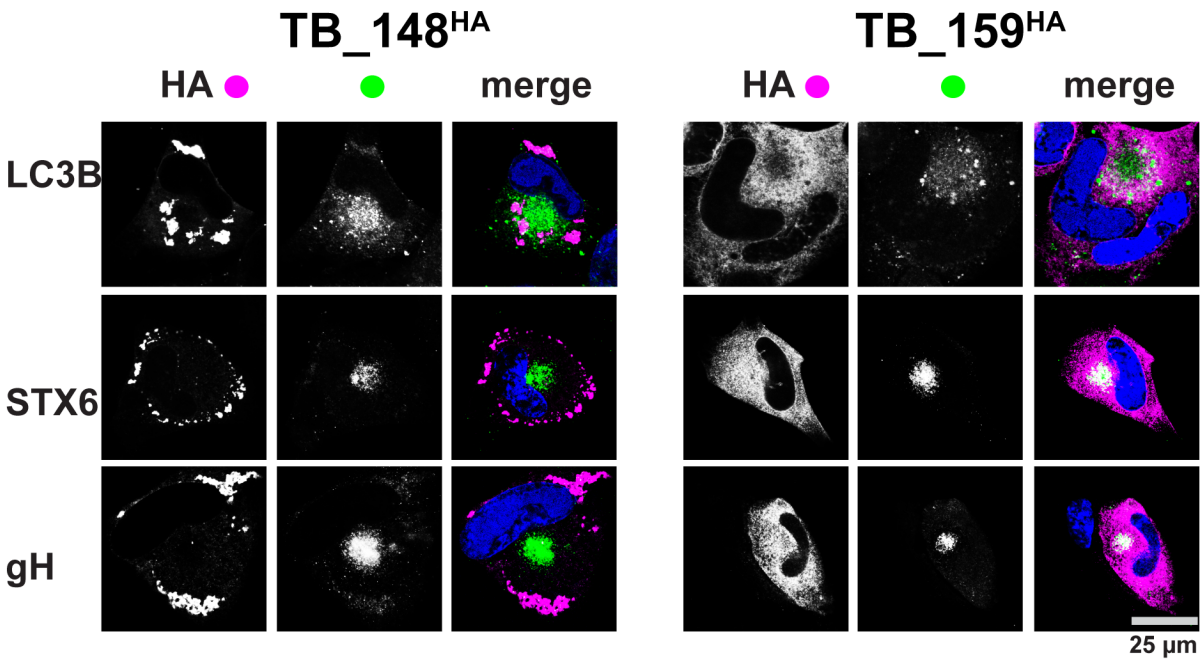

FIG S2: LC3B, syntaxin-6, and gH staining in HCMV infected cells. Human fibroblasts were infected with the indicated viruses for 96 h and then fixed, permeabilized, and stained using antibodies specific for the indicated proteins. Indirect immunofluorescence images were captured using a 63X objective on a Leica SP5 confocal microscope. gH: glycoprotein H, STX6: syntaxin-6.

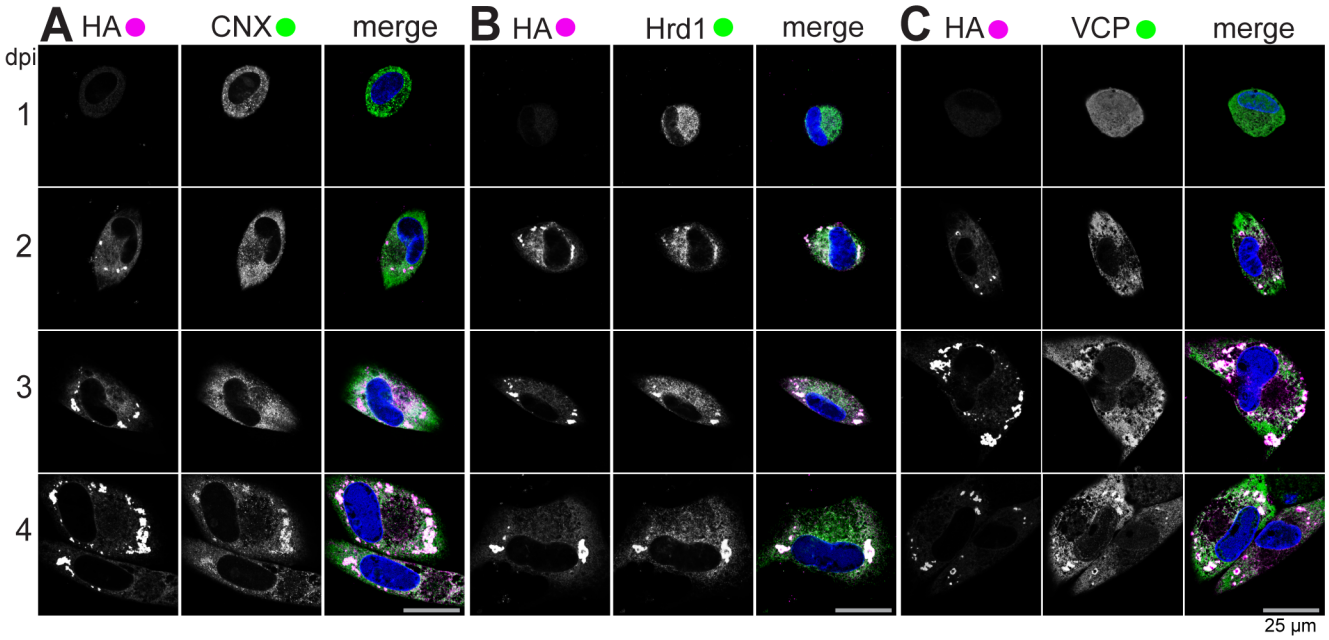

FIG S3: Cellular proteins involved in glycoprotein quality control are recruited with differing kinetics to UL148 ER structures. Fibroblasts infected with TB_148^{HA} at 1 MOI were fixed at the indicated time points (days post infection, dpi) and imaged by confocal microscopy after staining with antibodies specific for HA (UL148, magenta), CNX (green, **A**) , Hrd1 (green, **B**) or VCP(green, **C**), DAPI (blue).

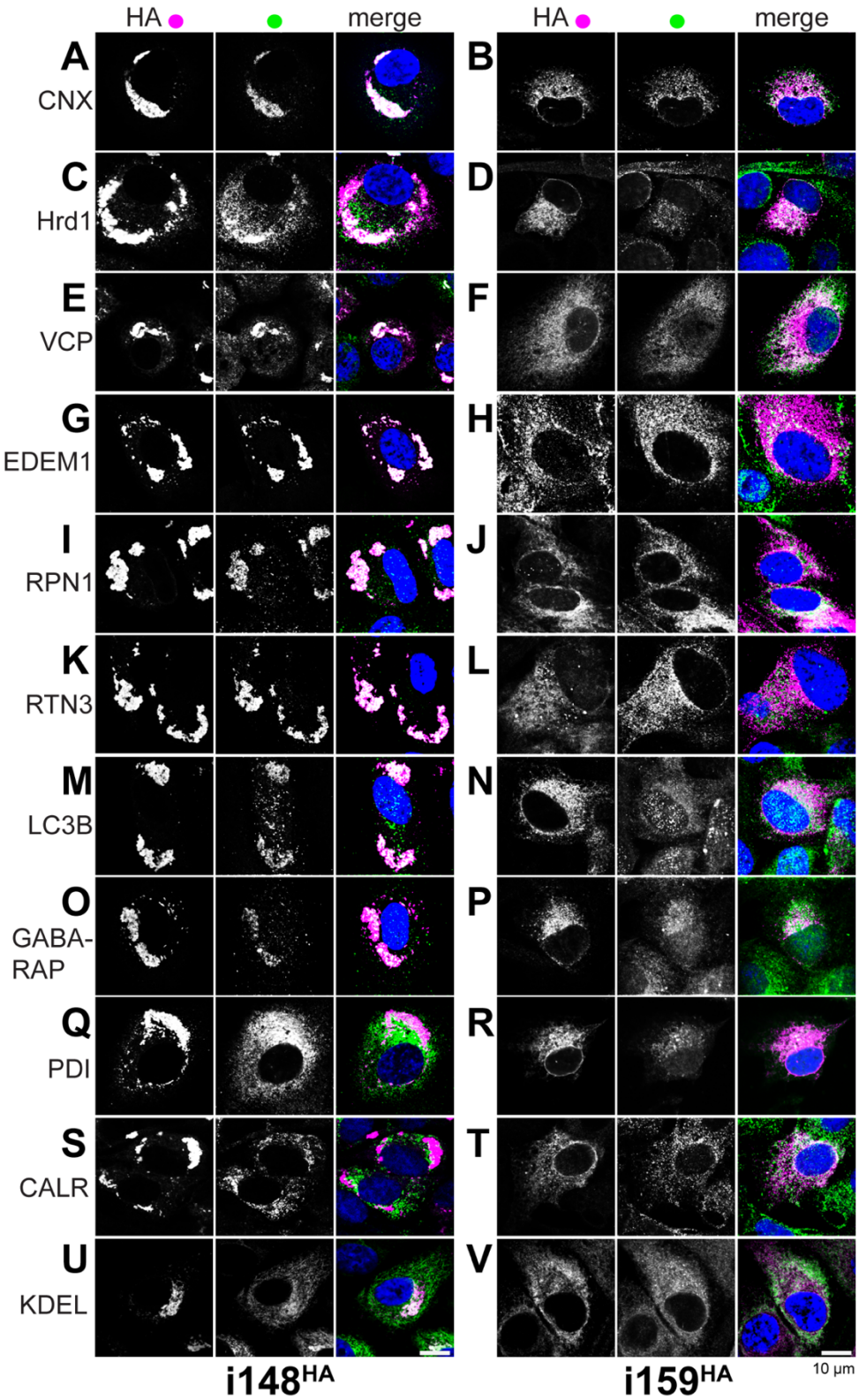

FIG S4. UL148 is sufficient to remodel the ER. Expression of HA-tagged UL148 or Rh159 was induced in "tet-on" ARPE-19 epithelial cells, i148^{HA} and i159^{HA}, respectively. Cells were fixed at 48 h postinduction for indirect immunofluorescence staining for the indicated cellular markers (green) together with HA (magenta). Scale bar: 10 µm.

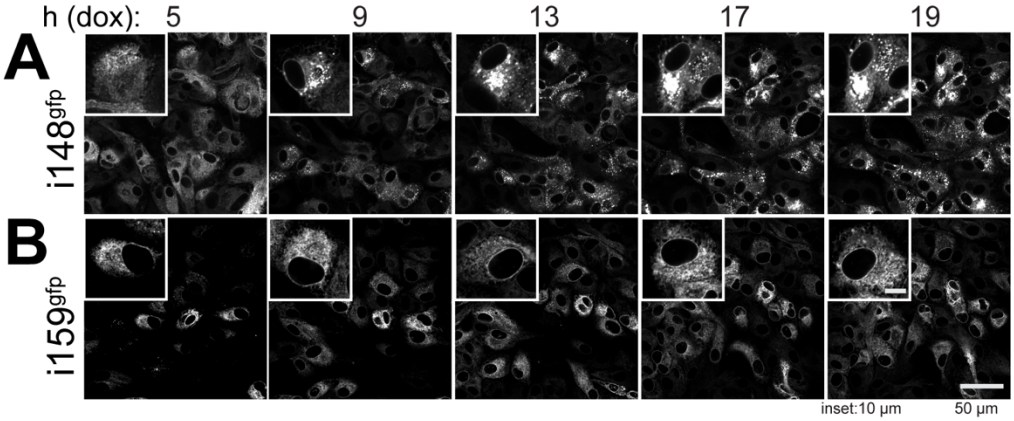

1066
1067
1068 **FIG S5. Live-cell Imaging of UL148-GFP and Rh159-GFP during induced ectopic**
1069 **expression.** "Tet-on" ARPE-19 epithelial cells that inducibly express either UL148 or Rh159
1070 fused to green florescent protein (gfp), i148^{gfp} (**A**) and i159^{gfp} (**B**), respectively, were induced for
1071 transgene expression using 100 ng/mL doxycycline (dox) and imaged using live-cell
1072 microscopy. Images from the selected time points (h post treatment with dox, hpt) are shown.
1073 The main scale bar represents 50 µm. For inset panels at upper left of each image, which are
1074 magnified 2.4× relative to the main image, the scale bar represents 10 µm. Also see SI Movies
1075 S2-S3.
1076
1077
1078
1079

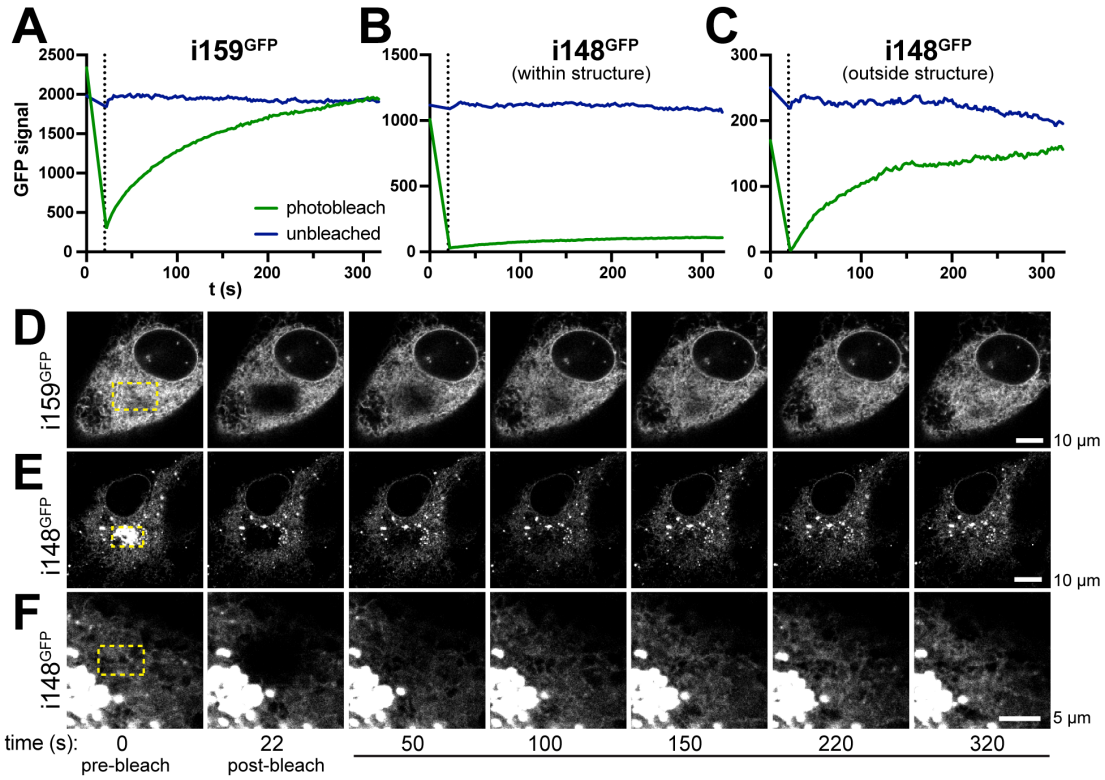

FIG S6. FRAP. ARPE-19 cells that inducibly express Rh159-GFP, i159^{gfp} (**A**) or UL148-GFP, i148^{gfp} (**B-C**) were doxycycline induced for 24 h (100 ng/mL doxycycline (dox). Separate regions of GFP signal in selected cells were photobleached (405 nm laser) or left unbleached, while a third region lacking GFP signal was chosen as a background reference were measured before and during fluorescence recovery after photobleaching (FRAP). Note: background signal was not plotted because values were resolvable from the x-axis. GFP signal intensity is plotted over a time period (seconds, s) starting with an exposure at t=0 (immediately before photobleaching), and including measurements taken every 2 s after photobleaching (0-20 s) until termination of the measurement series at t=322 s (300 s of FRAP). (**D-F**) Images from the selected time points (s, seconds) immediately before and after bleaching, and during fluorescence recovery period. Also see SI Movies S4-S6.

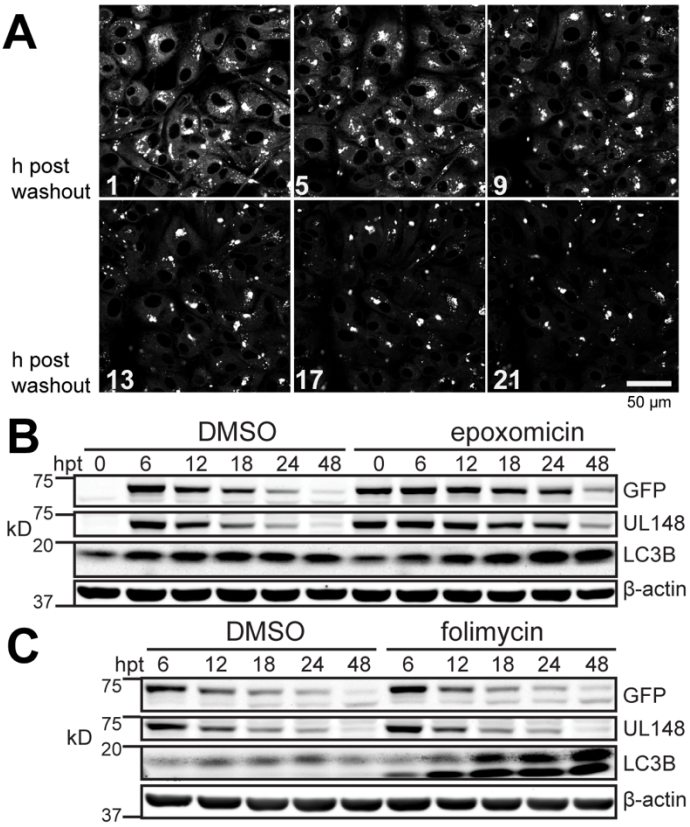

FIG S7: UL148-GFP is stabilized by inhibition of proteasomal but not lysosomal degradation. "Tet-on" ARPE-19 cells that inducibly express UL148-GFP (i148^{gfp}) were induced for 24 h by the addition of 100 ng/mL doxycycline (dox), after which the dox inducing agent was washed out and medium containing either the proteasome inhibitor epoxomicin (20 µM) or the proton pump inhibitor folimycin (115 nM) was added and samples were harvested for Western blot analysis at the indicated times post treatment (h post treatment, hpt) with folimycin or epoxomicin. DMSO was added at 0.1% to control for folimycin, or 1% to control for epoxomicin. Also see SI Movie S7.

TABLE S1. Oligonucleotide primers and synthetic DNAs.

Name	Sequence (5' to 3')
148_eGFP_Fw	ACCTGGTGTCGCGGCGTCGGATGGTGAGCAAGGGGGAGGAGCTTTTTACTGGCGTTGTTC
Gibs_eGFP_Rv	CGGCCGCCACTGTGCTGGATTACTTATACAGCTCGTCCATACCCAG
Gib_148_Fw	TGTGGTGGAATTCTGCAGATTGCCACCATGTTGCGCTTGCTG
148_noStopRv	CCGACGCCGCGACACCAGGTAGGTTATC
159_eGFP_Fw	TCTAAAACGCAGTCGTGAAGCTCATATGGTGAGCAAGGGGGAGGA
159_noStop_Rv	ATGAGCTTCACGACTGCGTTTTAGAAGTG
Gibs_159_Fw	TGTGGTGGAATTCTGCAGATTGCCACCATGGCCTACAACAGC
Rh159_Fw	TGTGGTGGAATTCTGCAGATACCATGGCCTACAACAGCTTCCTTCTCAGCTGCCTTACCATCGCAC TTTTACTG
Rh159_HA_Rv	CGGCCGCCACTGTGCTGGATCTATTAGGCGTAGTCTGGGACGTCGTATGGGTAATGAGCTTCACG ACTGCGTTTTAGAAGTG
PpuISceKanGibs_Fw	CATTCACCTGAACCCATAGGTCCTGCCTGGCAGAGAATCTTAGGGATAACAGGGTAATCG
PpuISceKanGibs _Rv	AGATTCTCTGCCAGGCAGGACCTATGGGTTCAGGTGAATGGCCAGTGTTACAACCAATTA
Rh159_Fw_recomb	GGGCGGTGGCCGGCACGCCGCATTTCCTAACCCGCGCAGCATGGCCTACAACAGCTTCCT
Rh159_Rv_recomb	CGCGAACGACGTGTGACGAGGACGTGGTTTCCGCAAGCCTTTAGGCGTAGTCTGGGACG
TB_159HAseq_F	AGTGTTTATGAGTCGGGCGG
TB_159HAseq_R	GTGGCGACGTGGATTTCTTG
EGFP-P2A-3XHA	GTCGACTGGATCCGGTACCGAATTCGCCACCATGGTGAGCAAGGGGGAGGAGCTTTTTACTGGC GTTGTTCCCATCCTGGTTGAGTTGGATGGGGATGTCAACGGCCACAAGTTCAGCGTTTCTGGAGA AGGAGAAGGCGACGCAACCTATGGGAAGCTCACTTTGAAATTCATATGCACCACCGGTAAACTCC CAGTCCCCTGGCCTACCCTGGTCACTACCTTGACATATGGAGTTCAGTGCTTTTCTCGATACCCCG ACCACATGAAGCAGCACGATTTTTTCAAATCTGCAATGCCCGAGGGCTATGTACAAGAGAGGACCA TTTTCTTCAAAGACGACGGCAATTACAAGACCAGGGCCGAGGTCAAATTTGAAGGGGACACTCTTG TGAATCGGATCGAACTTAAAGGGATCGATTTCAAAGAGGACGGAAACATACTGGGGCATAAGCTG GAATACAACTACAATAGCCATAATGTTTACATTATGGCAGACAAGCAGAAAAACGGTATTAAGGTCA ACTTCAAGATACGGCATAACATTGAAGATGGGTCAGTCCAGCTTGCTGACCATTATCAGCAGAATA CACCCATTGGCGATGGTCCCGTGCTTTTGCCTGACAACCACTACCTTTCTACCCAAAGCGCATTGT CAAAAGATCCTAACGAGAAGAGAGATCATATGGTCCTTTTGGAGTTCGTAACCGCAGCTGGTATAA CTCTGGGTATGGACGAGCTGTATAAGGGCTCAGGGGCTACAAATTTTAGTCTCCTTAAACAAGCCG GAGATGTCGAAGAGAACCCTGGGCCTTACCCATATGACGTTCCTGACTATGCCGGTTACCCCTAT GATGTGCCAGATTATGCCGGATCTTATCCTTACGATGTACCTGACTATGCAGGTGGGAGTGGCAT GAATTACGTGGGGCAGC
Gibs_Age_159_Fw	CCGTACCACTTCCTACCCTCGTAAACCGGTGCCACCATGGCCTACAACAG
Gibs_Mlu_GFP_Rv	ACCCGGCGCGGAGGCCAGATCTTAACGCGTTTACTTATACAGCTCGTCCATACC
tRFP linker Fw	CCACTTCCTACCCTCGTAAACCGGTGAATTCGCCACCATGAGCGAGCTGAT
tRFP linker Rv	GCGCGGAGGCCAGATCTTAACGCGTGCGGCCGCTCGAGAATTCATCTGTGCCCCAGTTTGC

1114
1115

TABLE S2. Antibodies Used in Immunofluorescence Microscopy

Primary Antibody	Host species	Isotype	Clone	Vendor	Catalog No.	Dilution used
Calnexin	Mouse	mAb IgG1	37	BD Biosciences	610523	1:50
Calnexin	Rabbit	mAb IgG	C5C9	Cell Signaling Tech.	2679	1:50
Syntaxin 6	Rabbit	mAb IgG	C34B2	Cell Signaling Tech.	2869	1:50
SYVN1 (Hrd1)	Rabbit	mAb IgG	D3O2A	Cell Signaling Tech.	14773	1:500
SEL1L	Rabbit	pAb	n/a	Sigma	S3699	1:50
KDEL	Mouse	IgG2a	10C3	Enzo Life Sci., Inc.	ADI-SPA-827-D	1:50
PDI	Rabbit	mAb IgG	C81H6	Cell Signaling Tech.	3501	1:50
Herp (HerpUD1)	Rabbit	pAb IgG	n/a	Proteintech	10813-1-AP	1:50
VCP	Mouse	IgG2a	5	Invitrogen / Life Technologies	MA3-004	1:50
Calreticulin	Rabbit	mAb IgG	D3E6	Cell Signaling Tech.	12238	1:200
Ribophorin 1 (RPN1)	Rabbit	pAb IgG		ThermoFisher / Invitrogen	PA5-65662	1:50
EDEM-1	Mouse	mAb IgM	D-1	Santa Cruz	sc-377394	1:50
GABARAP	Rabbit	mAb	E1J4E	Cell Signaling Tech.	13733	1:200
LC3B	Rabbit	mAb	D11	Cell Signaling Tech.	3868	1:200
HA epitope	Chicken	IgY		Bethyl	A190-106A	1:200
HCMV glycoprotein H (gH)	Mouse	IgG2b	14-4b	Gift of William J. Britt, M.D.	n/a	1: 50
Reticulon-3 (RTN3)	Mouse	IgG2a		ThermoFisher / Invitrogen	MA5-15538	1: 200
HA epitope	Rabbit	pAb		Bethyl	A190-108A	1:1000
Secondary Antibody	**Host species**	**Isotype**		**Vendor**	**Catalog No.**	**Dilution used**
Alexa Fluor 488 anti-Mouse IgG (H+L), cross adsorbed	Goat	IgG		ThermoFisher / Invitrogen	A11001	1:1000
Alexa Fluor 488 anti-Rabbit IgG (H+L) Cross-Adsorbed	Goat	IgG		ThermoFisher / Invitrogen	A11008	1:1000
Alexa Fluor 594 anti-Rabbit IgG (H+L) Cross-Adsorbed	Goat	IgG		ThermoFisher / Invitrogen	A11012	1:1000
Alexa Fluor 594 anti-Mouse IgG (H+L) Cross-Adsorbed	Goat	IgG		ThermoFisher / Invitrogen	A11005	1:1000
Alexa Fluor 647 anti-Chicken IgY (H+L)	Goat	IgG		ThermoFisher / Invitrogen	A11039	1:1000

1116
1117
1118

1119
1120
1121 **SUPPLEMENTARY VIDEO FILES.**
1122
1123 **Movie S1: STEM tomography of UL148 ER structures in wildtype HCMV infected**
1124 **fibroblasts at 5 dpi.**
1125
1126 **Movies S2 – S3: Live cell imaging of GFP signal following dox induction of transgene**
1127 **expression in i148^{gfp} and i159^{gfp} ARPE-19 epithelial cells.**
1128 **Movie S2: i148^{gfp} cells from 2-19 h post dox induction.**
1129 **Movie S3: i159^{gfp} cells from 2-19 h post dox induction.**
1130
1131 **Movies S4-S6: FRAP.**
1132 **Movie S4**: **FRAP of UL148-GFP structure (ER within structure).**
1133 **Movie S5: FRAP of UL148 GFP structure (ER outside structure).**
1134 **Movie S6: FRAP of Rh159-GFP.**
1135
1136 **Movie S7: Imaging of UL148-GFP following washout of doxycycline (dox):** live cell imaging
1137 capturing 30 min to 22 h 07 min post washout of dox**.**
1138
1139 **Movies S8-S10: ISR blockade.**
1140 **Movie S8: i148^{gfp} cells in the presence of 0.01% DMSO, from 2-19 h post dox induction.**
1141 **Movie S9: i148^{gfp} cells in the presence of 1.1 µM GSK2606414, from 2-19 h post dox**
1142 **induction.**
1143 **Movie S10: i148^{gfp} cells in the presence of 200 nM ISRIB, from 2-19 h post dox induction.**
1144
1145
1146
1147

1148 **REFERENCES.**

1149

1150 1. Li G, Nguyen CC, Ryckman BJ, Britt WJ, Kamil JP. 2015. A viral regulator of glycoprotein
1151 complexes contributes to human cytomegalovirus cell tropism. Proc Natl Acad Sci U S A
1152 112:4471-6.
1153 2. Wille PT, Knoche AJ, Nelson JA, Jarvis MA, Johnson DC. 2010. A human cytomegalovirus
1154 gO-null mutant fails to incorporate gH/gL into the virion envelope and is unable to enter
1155 fibroblasts and epithelial and endothelial cells. J Virol 84:2585-96.
1156 3. Jiang XJ, Adler B, Sampaio KL, Digel M, Jahn G, Ettischer N, Stierhof YD, Scrivano L,
1157 Koszinowski U, Mach M, Sinzger C. 2008. UL74 of human cytomegalovirus contributes to
1158 virus release by promoting secondary envelopment of virions. J Virol 82:2802-12.
1159 4. Zhou M, Lanchy JM, Ryckman BJ. 2015. Human Cytomegalovirus gH/gL/gO Promotes the
1160 Fusion Step of Entry into All Cell Types, whereas gH/gL/UL128-131 Broadens Virus
1161 Tropism through a Distinct Mechanism. J Virol 89:8999-9009.
1162 5. Wu Y, Prager A, Boos S, Resch M, Brizic I, Mach M, Wildner S, Scrivano L, Adler B. 2017.
1163 Human cytomegalovirus glycoprotein complex gH/gL/gO uses PDGFR-alpha as a key for
1164 entry. PLoS Pathog 13:e1006281.
1165 6. Kabanova A, Marcandalli J, Zhou T, Bianchi S, Baxa U, Tsybovsky Y, Lilleri D, Silacci-Fregni
1166 C, Foglierini M, Fernandez-Rodriguez BM, Druz A, Zhang B, Geiger R, Pagani M, Sallusto
1167 F, Kwong PD, Corti D, Lanzavecchia A, Perez L. 2016. Platelet-derived growth factor-
1168 alpha receptor is the cellular receptor for human cytomegalovirus gHgLgO trimer. Nat
1169 Microbiol 1:16082.
1170 7. Wu K, Oberstein A, Wang W, Shenk T. 2018. Role of PDGF receptor-alpha during human
1171 cytomegalovirus entry into fibroblasts. Proc Natl Acad Sci U S A
1172 doi:10.1073/pnas.1806305115.
1173 8. Nguyen CC, Siddiquey MNA, Zhang H, Li G, Kamil JP. 2018. Human Cytomegalovirus
1174 Tropism Modulator UL148 Interacts with SEL1L, a Cellular Factor That Governs
1175 Endoplasmic Reticulum-Associated Degradation of the Viral Envelope Glycoprotein gO. J
1176 Virol 92:e00688-18.
1177 9. Wang ECY, Pjechova M, Nightingale K, Vlahava VM, Patel M, Ruckova E, Forbes SK,
1178 Nobre L, Antrobus R, Roberts D, Fielding CA, Seirafian S, Davies J, Murrell I, Lau B, Wilkie
1179 GS, Suarez NM, Stanton RJ, Vojtesek B, Davison A, Lehner PJ, Weekes MP, Wilkinson
1180 GWG, Tomasec P. 2018. Suppression of costimulation by human cytomegalovirus
1181 promotes evasion of cellular immune defenses. Proc Natl Acad Sci U S A 115:4998-5003.
1182 10. Siddiquey MNA, Zhang H, Nguyen CC, Domma AJ, Kamil JP. 2018. The Human
1183 Cytomegalovirus Endoplasmic Reticulum-Resident Glycoprotein UL148 Activates the
1184 Unfolded Protein Response. J Virol 92:e00896-18.
1185 11. Sinzger C, Hahn G, Digel M, Katona R, Sampaio KL, Messerle M, Hengel H, Koszinowski U,
1186 Brune W, Adler B. 2008. Cloning and sequencing of a highly productive, endotheliotropic
1187 virus strain derived from human cytomegalovirus TB40/E. J Gen Virol 89:359-68.
1188 12. Das S, Vasanji A, Pellett PE. 2007. Three-dimensional structure of the human
1189 cytomegalovirus cytoplasmic virion assembly complex includes a reoriented secretory
1190 apparatus. J Virol 81:11861-9.

1191 13. Sanchez V, Greis KD, Sztul E, Britt WJ. 2000. Accumulation of virion tegument and
1192 envelope proteins in a stable cytoplasmic compartment during human cytomegalovirus
1193 replication: characterization of a potential site of virus assembly. J Virol 74:975-86.
1194 14. Lilley BN, Ploegh HL. 2005. Multiprotein complexes that link dislocation, ubiquitination,
1195 and extraction of misfolded proteins from the endoplasmic reticulum membrane. Proc
1196 Natl Acad Sci U S A 102:14296-301.
1197 15. Kamhi-Nesher S, Shenkman M, Tolchinsky S, Fromm SV, Ehrlich R, Lederkremer GZ.
1198 2001. A novel quality control compartment derived from the endoplasmic reticulum.
1199 Mol Biol Cell 12:1711-23.
1200 16. Leitman J, Shenkman M, Gofman Y, Shtern NO, Ben-Tal N, Hendershot LM, Lederkremer
1201 GZ. 2014. Herp coordinates compartmentalization and recruitment of HRD1 and
1202 misfolded proteins for ERAD. Mol Biol Cell 25:1050-60.
1203 17. Houck SA, Ren HY, Madden VJ, Bonner JN, Conlin MP, Janovick JA, Conn PM, Cyr DM.
1204 2014. Quality control autophagy degrades soluble ERAD-resistant conformers of the
1205 misfolded membrane protein GnRHR. Mol Cell 54:166-179.
1206 18. Sturgill ER, Malouli D, Hansen SG, Burwitz BJ, Seo S, Schneider CL, Womack JL, Verweij
1207 MC, Ventura AB, Bhusari A, Jeffries KM, Legasse AW, Axthelm MK, Hudson AW, Sacha
1208 JB, Picker LJ, Fruh K. 2016. Natural Killer Cell Evasion Is Essential for Infection by Rhesus
1209 Cytomegalovirus. PLoS Pathog 12:e1005868.
1210 19. Chaumorcel M, Souquere S, Pierron G, Codogno P, Esclatine A. 2008. Human
1211 cytomegalovirus controls a new autophagy-dependent cellular antiviral defense
1212 mechanism. Autophagy 4:46-53.
1213 20. Chaumorcel M, Lussignol M, Mouna L, Cavignac Y, Fahie K, Cotte-Laffitte J, Geballe A,
1214 Brune W, Beau I, Codogno P, Esclatine A. 2012. The human cytomegalovirus protein
1215 TRS1 inhibits autophagy via its interaction with Beclin 1. J Virol 86:2571-84.
1216 21. Alwine JC. 2012. The human cytomegalovirus assembly compartment: a masterpiece of
1217 viral manipulation of cellular processes that facilitates assembly and egress. PLoS Pathog
1218 8:e1002878.
1219 22. Das S, Pellett PE. 2011. Spatial relationships between markers for secretory and
1220 endosomal machinery in human cytomegalovirus-infected cells versus those in
1221 uninfected cells. J Virol 85:5864-79.
1222 23. Leitman J, Ron E, Ogen-Shtern N, Lederkremer GZ. 2013. Compartmentalization of
1223 endoplasmic reticulum quality control and ER-associated degradation factors. DNA Cell
1224 Biol 32:2-7.
1225 24. Cox DW, Billingsley GD, Callahan JW. 1986. Aggregation of plasma Z type alpha 1-
1226 antitrypsin suggests basic defect for the deficiency. FEBS Lett 205:255-60.
1227 25. Le A, Ferrell GA, Dishon DS, Le QQ, Sifers RN. 1992. Soluble aggregates of the human PiZ
1228 alpha 1-antitrypsin variant are degraded within the endoplasmic reticulum by a
1229 mechanism sensitive to inhibitors of protein synthesis. J Biol Chem 267:1072-80.
1230 26. Lomas DA, Evans DL, Finch JT, Carrell RW. 1992. The mechanism of Z alpha 1-antitrypsin
1231 accumulation in the liver. Nature 357:605-7.
1232 27. Ordonez A, Snapp EL, Tan L, Miranda E, Marciniak SJ, Lomas DA. 2013. Endoplasmic
1233 reticulum polymers impair luminal protein mobility and sensitize to cellular stress in
1234 alpha1-antitrypsin deficiency. Hepatology 57:2049-60.

1235 28. Ekeowa UI, Freeke J, Miranda E, Gooptu B, Bush MF, Perez J, Teckman J, Robinson CV,
1236 Lomas DA. 2010. Defining the mechanism of polymerization in the serpinopathies. Proc
1237 Natl Acad Sci U S A 107:17146-51.
1238 29. Suhy DA, Giddings TH, Jr., Kirkegaard K. 2000. Remodeling the endoplasmic reticulum by
1239 poliovirus infection and by individual viral proteins: an autophagy-like origin for virus-
1240 induced vesicles. J Virol 74:8953-65.
1241 30. Windsor M, Hawes P, Monaghan P, Snapp E, Salas ML, Rodriguez JM, Wileman T. 2012.
1242 Mechanism of collapse of endoplasmic reticulum cisternae during African swine fever
1243 virus infection. Traffic 13:30-42.
1244 31. Miller S, Krijnse-Locker J. 2008. Modification of intracellular membrane structures for
1245 virus replication. Nat Rev Microbiol 6:363-74.
1246 32. Siddiquey MNA, Zhang H, Nguyen CC, Domma AJ, Kamil JP. 2018. The human
1247 cytomegalovirus ER resident glycoprotein UL148 activates the unfolded protein
1248 response. J Virol doi:10.1128/JVI.00896-18.
1249 33. Cormack BP, Valdivia RH, Falkow S. 1996. FACS-optimized mutants of the green
1250 fluorescent protein (GFP). Gene 173:33-8.
1251 34. Khaminets A, Heinrich T, Mari M, Grumati P, Huebner AK, Akutsu M, Liebmann L, Stolz
1252 A, Nietzsche S, Koch N, Mauthe M, Katona I, Qualmann B, Weis J, Reggiori F, Kurth I,
1253 Hubner CA, Dikic I. 2015. Regulation of endoplasmic reticulum turnover by selective
1254 autophagy. Nature 522:354-8.
1255 35. Meng L, Mohan R, Kwok BH, Elofsson M, Sin N, Crews CM. 1999. Epoxomicin, a potent
1256 and selective proteasome inhibitor, exhibits in vivo antiinflammatory activity. Proc Natl
1257 Acad Sci U S A 96:10403-8.
1258 36. Muroi M, Shiragami N, Nagao K, Yamasaki M, Takatsuki A. 1993. Folimycin
1259 (concanamycin A), a specific inhibitor of V-ATPase, blocks intracellular translocation of
1260 the glycoprotein of vesicular stomatitis virus before arrival to the Golgi apparatus. Cell
1261 Struct Funct 18:139-49.
1262 37. Muroi M, Takasu A, Yamasaki M, Takatsuki A. 1993. Folimycin (concanamycin A), an
1263 inhibitor of V-type H(+)-ATPase, blocks cell-surface expression of virus-envelope
1264 glycoproteins. Biochem Biophys Res Commun 193:999-1005.
1265 38. Kondratyev M, Avezov E, Shenkman M, Groisman B, Lederkremer GZ. 2007. PERK-
1266 dependent compartmentalization of ERAD and unfolded protein response machineries
1267 during ER stress. Exp Cell Res 313:3395-407.
1268 39. Harding HP, Novoa I, Zhang Y, Zeng H, Wek R, Schapira M, Ron D. 2000. Regulated
1269 translation initiation controls stress-induced gene expression in mammalian cells. Mol
1270 Cell 6:1099-108.
1271 40. Palam LR, Baird TD, Wek RC. 2011. Phosphorylation of eIF2 facilitates ribosomal bypass
1272 of an inhibitory upstream ORF to enhance CHOP translation. J Biol Chem 286:10939-49.
1273 41. Vattem KM, Wek RC. 2004. Reinitiation involving upstream ORFs regulates ATF4 mRNA
1274 translation in mammalian cells. Proc Natl Acad Sci U S A 101:11269-74.
1275 42. Sidrauski C, Acosta-Alvear D, Khoutorsky A, Vedantham P, Hearn BR, Li H, Gamache K,
1276 Gallagher CM, Ang KK, Wilson C, Okreglak V, Ashkenazi A, Hann B, Nader K, Arkin MR,
1277 Renslo AR, Sonenberg N, Walter P. 2013. Pharmacological brake-release of mRNA
1278 translation enhances cognitive memory. Elife 2:e00498.

1279 43. Sidrauski C, McGeachy AM, Ingolia NT, Walter P. 2015. The small molecule ISRIB
1280 reverses the effects of eIF2alpha phosphorylation on translation and stress granule
1281 assembly. Elife 4.
1282 44. Zyryanova AF, Weis F, Faille A, Alard AA, Crespillo-Casado A, Sekine Y, Harding HP, Allen
1283 F, Parts L, Fromont C, Fischer PM, Warren AJ, Ron D. 2018. Binding of ISRIB reveals a
1284 regulatory site in the nucleotide exchange factor eIF2B. Science 359:1533-1536.
1285 45. Sidrauski C, Tsai JC, Kampmann M, Hearn BR, Vedantham P, Jaishankar P, Sokabe M,
1286 Mendez AS, Newton BW, Tang EL, Verschueren E, Johnson JR, Krogan NJ, Fraser CS,
1287 Weissman JS, Renslo AR, Walter P. 2015. Pharmacological dimerization and activation of
1288 the exchange factor eIF2B antagonizes the integrated stress response. Elife 4:e07314.
1289 46. Tsai JC, Miller-Vedam LE, Anand AA, Jaishankar P, Nguyen HC, Renslo AR, Frost A, Walter
1290 P. 2018. Structure of the nucleotide exchange factor eIF2B reveals mechanism of
1291 memory-enhancing molecule. Science 359.
1292 47. Gordiyenko Y, Schmidt C, Jennings MD, Matak-Vinkovic D, Pavitt GD, Robinson CV. 2014.
1293 eIF2B is a decameric guanine nucleotide exchange factor with a gamma2epsilon2
1294 tetrameric core. Nat Commun 5:3902.
1295 48. Harding HP, Zhang Y, Ron D. 1999. Protein translation and folding are coupled by an
1296 endoplasmic-reticulum-resident kinase. Nature 397:271-4.
1297 49. Harding HP, Zhang Y, Bertolotti A, Zeng H, Ron D. 2000. Perk is essential for translational
1298 regulation and cell survival during the unfolded protein response. Mol Cell 5:897-904.
1299 50. Axten JM, Medina JR, Feng Y, Shu A, Romeril SP, Grant SW, Li WH, Heerding DA,
1300 Minthorn E, Mencken T, Atkins C, Liu Q, Rabindran S, Kumar R, Hong X, Goetz A, Stanley
1301 T, Taylor JD, Sigethy SD, Tomberlin GH, Hassell AM, Kahler KM, Shewchuk LM, Gampe
1302 RT. 2012. Discovery of 7-methyl-5-(1-{[3-(trifluoromethyl)phenyl]acetyl}-2,3-dihydro-1H-
1303 indol-5-yl)-7H-p yrrolo[2,3-d]pyrimidin-4-amine (GSK2606414), a potent and selective
1304 first-in-class inhibitor of protein kinase R (PKR)-like endoplasmic reticulum kinase
1305 (PERK). J Med Chem 55:7193-207.
1306 51. Tenorio R, Fernandez de Castro I, Knowlton JJ, Zamora PF, Lee CH, Mainou BA, Dermody
1307 TS, Risco C. 2018. Reovirus sigmaNS and muNS Proteins Remodel the Endoplasmic
1308 Reticulum to Build Replication Neo-Organelles. MBio 9.
1309 52. Miller S, Kastner S, Krijnse-Locker J, Buhler S, Bartenschlager R. 2007. The non-structural
1310 protein 4A of dengue virus is an integral membrane protein inducing membrane
1311 alterations in a 2K-regulated manner. J Biol Chem 282:8873-82.
1312 53. Lamond AI, Sleeman JE. 2003. Nuclear substructure and dynamics. Curr Biol 13:R825-8.
1313 54. Granell S, Baldini G, Mohammad S, Nicolin V, Narducci P, Storrie B, Baldini G. 2008.
1314 Sequestration of mutated alpha1-antitrypsin into inclusion bodies is a cell-protective
1315 mechanism to maintain endoplasmic reticulum function. Mol Biol Cell 19:572-86.
1316 55. Lawless MW, Greene CM, Mulgrew A, Taggart CC, O'Neill SJ, McElvaney NG. 2004.
1317 Activation of endoplasmic reticulum-specific stress responses associated with the
1318 conformational disease Z alpha 1-antitrypsin deficiency. J Immunol 172:5722-6.
1319 56. Tirosh B, Iwakoshi NN, Lilley BN, Lee AH, Glimcher LH, Ploegh HL. 2005. Human
1320 cytomegalovirus protein US11 provokes an unfolded protein response that may
1321 facilitate the degradation of class I major histocompatibility complex products. J Virol
1322 79:2768-79.

1323 57. Wiertz EJ, Jones TR, Sun L, Bogyo M, Geuze HJ, Ploegh HL. 1996. The human
1324 cytomegalovirus US11 gene product dislocates MHC class I heavy chains from the
1325 endoplasmic reticulum to the cytosol. Cell 84:769-79.
1326 58. van den Boomen DJ, Timms RT, Grice GL, Stagg HR, Skodt K, Dougan G, Nathan JA,
1327 Lehner PJ. 2014. TMEM129 is a Derlin-1 associated ERAD E3 ligase essential for virus-
1328 induced degradation of MHC-I. Proc Natl Acad Sci U S A 111:11425-30.
1329 59. Caramelo JJ, Parodi AJ. 2008. Getting in and out from calnexin/calreticulin cycles. J Biol
1330 Chem 283:10221-5.
1331 60. Hammond C, Braakman I, Helenius A. 1994. Role of N-linked oligosaccharide
1332 recognition, glucose trimming, and calnexin in glycoprotein folding and quality control.
1333 Proc Natl Acad Sci U S A 91:913-7.
1334 61. Zhou M, Yu Q, Wechsler A, Ryckman BJ. 2013. Comparative analysis of gO isoforms
1335 reveals that strains of human cytomegalovirus differ in the ratio of gH/gL/gO and
1336 gH/gL/UL128-131 in the virion envelope. J Virol 87:9680-90.
1337 62. Zhang L, Zhou M, Stanton R, Kamil J, Ryckman BJ. 2018. Expression Levels of
1338 Glycoprotein O (gO) Vary between Strains of Human Cytomegalovirus, Influencing the
1339 Assembly of gH/gL Complexes and Virion Infectivity. J Virol 92.
1340 63. Sifers RN, Brashears-Macatee S, Kidd VJ, Muensch H, Woo SL. 1988. A frameshift
1341 mutation results in a truncated alpha 1-antitrypsin that is retained within the rough
1342 endoplasmic reticulum. J Biol Chem 263:7330-5.
1343 64. Choudhury P, Liu Y, Bick RJ, Sifers RN. 1997. Intracellular association between UDP-
1344 glucose:glycoprotein glucosyltransferase and an incompletely folded variant of alpha1-
1345 antitrypsin. J Biol Chem 272:13446-51.
1346 65. Tsao YS, Ivessa NE, Adesnik M, Sabatini DD, Kreibich G. 1992. Carboxy terminally
1347 truncated forms of ribophorin I are degraded in pre-Golgi compartments by a calcium-
1348 dependent process. J Cell Biol 116:57-67.
1349 66. de Virgilio M, Weninger H, Ivessa NE. 1998. Ubiquitination is required for the retro-
1350 translocation of a short-lived luminal endoplasmic reticulum glycoprotein to the cytosol
1351 for degradation by the proteasome. J Biol Chem 273:9734-43.
1352 67. Johnston JA, Ward CL, Kopito RR. 1998. Aggresomes: a cellular response to misfolded
1353 proteins. J Cell Biol 143:1883-98.
1354 68. Johnston JA, Illing ME, Kopito RR. 2002. Cytoplasmic dynein/dynactin mediates the
1355 assembly of aggresomes. Cell Motil Cytoskeleton 53:26-38.
1356 69. Pankiv S, Alemu EA, Brech A, Bruun JA, Lamark T, Overvatn A, Bjorkoy G, Johansen T.
1357 2010. FYCO1 is a Rab7 effector that binds to LC3 and PI3P to mediate microtubule plus
1358 end-directed vesicle transport. J Cell Biol 188:253-69.
1359 70. Hummel T, Krukkert K, Roos J, Davis G, Klambt C. 2000. Drosophila Futsch/22C10 is a
1360 MAP1B-like protein required for dendritic and axonal development. Neuron 26:357-70.
1361 71. Wang H, Bedford FK, Brandon NJ, Moss SJ, Olsen RW. 1999. GABA(A)-receptor-
1362 associated protein links GABA(A) receptors and the cytoskeleton. Nature 397:69-72.
1363 72. Zhang K, Daigle JG, Cunningham KM, Coyne AN, Ruan K, Grima JC, Bowen KE, Wadhwa
1364 H, Yang P, Rigo F, Taylor JP, Gitler AD, Rothstein JD, Lloyd TE. 2018. Stress Granule
1365 Assembly Disrupts Nucleocytoplasmic Transport. Cell 173:958-971 e17.

1366 73. Li YR, King OD, Shorter J, Gitler AD. 2013. Stress granules as crucibles of ALS
1367 pathogenesis. J Cell Biol 201:361-72.
1368 74. Hetz C, Saxena S. 2017. ER stress and the unfolded protein response in
1369 neurodegeneration. Nat Rev Neurol 13:477-491.
1370 75. Kirchoff V, Wong S, St JS, Pari GS. 2002. Generation of a life-expanded rhesus monkey
1371 fibroblast cell line for the growth of rhesus rhadinovirus (RRV). Arch Virol 147:321-33.
1372 76. Smith IL, Taskintuna I, Rahhal FM, Powell HC, Ai E, Mueller AJ, Spector SA, Freeman WR.
1373 1998. Clinical failure of CMV retinitis with intravitreal cidofovir is associated with
1374 antiviral resistance. Arch Ophthalmol 116:178-85.
1375 77. Murphy E, Yu D, Grimwood J, Schmutz J, Dickson M, Jarvis MA, Hahn G, Nelson JA,
1376 Myers RM, Shenk TE. 2003. Coding potential of laboratory and clinical strains of human
1377 cytomegalovirus. Proc Natl Acad Sci U S A 100:14976-81.
1378 78. Stanton RJ, Baluchova K, Dargan DJ, Cunningham C, Sheehy O, Seirafian S, McSharry BP,
1379 Neale ML, Davies JA, Tomasec P, Davison AJ, Wilkinson GW. 2010. Reconstruction of the
1380 complete human cytomegalovirus genome in a BAC reveals RL13 to be a potent inhibitor
1381 of replication. J Clin Invest 120:3191-208.
1382 79. Hobom U, Brune W, Messerle M, Hahn G, Koszinowski UH. 2000. Fast screening
1383 procedures for random transposon libraries of cloned herpesvirus genomes: mutational
1384 analysis of human cytomegalovirus envelope glycoprotein genes. J Virol 74:7720-9.
1385 80. Chang WL, Barry PA. 2003. Cloning of the full-length rhesus cytomegalovirus genome as
1386 an infectious and self-excisable bacterial artificial chromosome for analysis of viral
1387 pathogenesis. J Virol 77:5073-83.
1388 81. Tischer BK, Smith GA, Osterrieder N. 2010. En passant mutagenesis: a two step
1389 markerless red recombination system. Methods Mol Biol 634:421-30.
1390 82. Tischer BK, von Einem J, Kaufer B, Osterrieder N. 2006. Two-step red-mediated
1391 recombination for versatile high-efficiency markerless DNA manipulation in Escherichia
1392 coli. Biotechniques 40:191-7.
1393 83. Dietz AN, Villinger C, Becker S, Frick M, von Einem J. 2018. A Tyrosine-Based Trafficking
1394 Motif of the Tegument Protein pUL71 Is Crucial for Human Cytomegalovirus Secondary
1395 Envelopment. J Virol 92.
1396 84. Hohn K, Sailer M, Wang L, Lorenz M, Schneider ME, Walther P. 2011. Preparation of
1397 cryofixed cells for improved 3D ultrastructure with scanning transmission electron
1398 tomography. Histochem Cell Biol 135:1-9.
1399 85. Villinger C, Schauflinger M, Gregorius H, Kranz C, Hohn K, Nafeey S, Walther P. 2014.
1400 Three-dimensional imaging of adherent cells using FIB/SEM and STEM. Methods Mol
1401 Biol 1117:617-38.
1402 86. Kremer JR, Mastronarde DN, McIntosh JR. 1996. Computer visualization of three-
1403 dimensional image data using IMOD. J Struct Biol 116:71-6.
1404 87. Britt WJ, Jarvis MA, Drummond DD, Mach M. 2005. Antigenic domain 1 is required for
1405 oligomerization of human cytomegalovirus glycoprotein B. J Virol 79:4066-79.
1406

1407